J Atmos Chem (2010) 67:87–140
DOI 10.1007/s10874-011-9206-1

Seasonal characteristics of tropical marine boundary layer air measured at the Cape Verde Atmospheric Observatory

L. J. Carpenter · Z. L. Fleming · K. A. Read · J. D. Lee · S. J. Moller · J. R. Hopkins · R. M. Purvis · A. C. Lewis · K. Müller · B. Heinold · H. Herrmann · K. Wadinga Fomba · D. van Pinxteren · C. Müller · I. Tegen · A. Wiedensohler · T. Müller · N. Niedermeier · E. P. Achterberg · M. D. Patey · E. A. Kozlova · M. Heimann · D. E. Heard · J. M. C. Plane · A. Mahajan · H. Oetjen · T. Ingham · D. Stone · L. K. Whalley · M. J. Evans · M. J. Pilling · R. J. Leigh · P. S. Monks · A. Karunaharan · S. Vaughan · S. R. Arnold · J. Tschritter · D. Pöhler · U. Frieß · R. Holla · L. M. Mendes · H. Lopez · B. Faria · A. J. Manning · D. W. R. Wallace

Received: 25 May 2011 / Accepted: 24 October 2011 /

Abstract Observations of the tropical atmosphere are fundamental to the understanding of global changes in air quality, atmospheric oxidation capacity and climate, yet the tropics are under-populated with long-term measurements. The first three years (October 2006–September 2009) of meteorological, trace gas and particulate data from the global WMO/Global Atmospheric Watch (GAW) Cape Verde Atmospheric Observatory Humberto Duarte Fonseca

---

L. J. Carpenter (✉) · K. A. Read · J. D. Lee · S. J. Moller · J. R. Hopkins · R. M. Purvis · A. C. Lewis
National Centre for Atmospheric Science, Department of Chemistry, University of York,
York YO10 5DD, UK
e-mail: lucy.carpenter@york.ac.uk

Z. L. Fleming
National Centre for Atmospheric Science, Department of Chemistry, University of Leicester,
Leicester LE1 7RH, UK

P. S. Monks · A. Karunaharan
Department of Chemistry, University of Leicester, Leicester LE1 7RH, UK

K. Müller · B. Heinold · H. Herrmann · K. W. Fomba · D. van Pinxteren · C. Müller · I. Tegen ·
A. Wiedensohler · T. Müller · N. Niedermeier
Leibniz-Institut für Troposphärenforschung e.V., Permoserstr. 15, 04318 Leipzig, Germany

E. P. Achterberg · M. D. Patey
School of Ocean and Earth Science, National Oceanography Centre Southampton,
University of Southampton, Southampton SO14 3ZH, UK

E. A. Kozlova · M. Heimann
Max-Planck-Institut für Biogeochemie, Jena, Germany

(CVAO; 16° 51′ N, 24° 52′ W) are presented, along with a characterisation of the origin and pathways of air masses arriving at the station using the NAME dispersion model and simulations of dust deposition using the COSMO-MUSCAT dust model. The observations show a strong influence from Saharan dust in winter with a maximum in super-micron aerosol and particulate iron and aluminium. The dust model results match the magnitude and daily variations of dust events, but in the region of the CVAO underestimate the measured aerosol optical thickness (AOT) because of contributions from other aerosol. The NAME model also captured the dust events, giving confidence in its ability to correctly identify air mass origins and pathways in this region. Dissolution experiments on collected dust samples showed a strong correlation between soluble Fe and Al and measured solubilities were lower at high atmospheric dust concentrations. Fine mode aerosol at the CVAO contains a significant fraction of non-sea salt components including dicarboxylic acids, methanesulfonic acid and aliphatic amines, all believed to be of oceanic origin. A marine influence is also apparent in the year-round presence of iodine and bromine monoxide (IO and BrO), with IO suggested to be

---

D. E. Heard · J. M. C. Plane · A. Mahajan · H. Oetjen · D. Stone · M. J. Pilling · S. Vaughan
School of Chemistry, University of Leeds, Leeds LS2 9JT, UK

T. Ingham · L. K. Whalley
National Centre for Atmospheric Science, School of Chemistry, University of Leeds, Leeds LS2 9JT, UK

D. Stone · M. J. Evans · S. R. Arnold
Institute for Climate & Atmospheric Science, School of Earth & Environment, University of Leeds,
Leeds LS2 9JT, UK

R. J. Leigh
Earth Observation Science, Department of Physics & Astronomy, University of Leicester, Leicester, UK

J. Tschritter · D. Pöhler · U. Frieß · R. Holla
Institute of Environmental Physics, University of Heidelberg, Heidelberg, Germany

L. M. Mendes · H. Lopez · B. Faria
Instituto Nacional de Meteorologia e Geofísica (INMG), Mindelo, Sao Vicente, Cape Verde

A. J. Manning
The Met Office, Exeter, Devon EX1 3PB, UK

D. W. R. Wallace
Leibniz-Institut für Meereswissenschaften (IFM-GEOMAR) Marine Biogeochemie,
Düsternbrooker Weg 20, 24105 Kiel, Germany

Present Address:
E. A. Kozlova
School of Environmental Sciences, University of East Anglia (UEA), Norwich, UK

Present Address:
A. Mahajan
Laboratorio de Ciencias de la Atmósfera y el Clima (CIAC), Toledo, Spain

Present Address:
H. Oetjen
Department of Chemistry, University of Colorado, Boulder, CO 80309, USA

Present Address:
M. J. Evans
Department of Chemistry, University of York, York YO10 5DD, UK

confined mainly to the surface few hundred metres but BrO well mixed in the boundary layer. Enhanced CO_2 and CH_4 and depleted oxygen concentrations are markers for air-sea exchange over the nearby northwest African coastal upwelling area. Long-range transport results in generally higher levels of O_3 and anthropogenic non-methane hydrocarbons (NMHC) in air originating from North America. Ozone/CO ratios were highest (up to 0.42) in relatively fresh European air masses. In air heavily influenced by Saharan dust the O_3/CO ratio was as low as 0.13, possibly indicating O_3 uptake to dust. Nitrogen oxides (NO_x and NO_y) show generally higher concentrations in winter when air mass origins are predominantly from Africa. High photochemical activity at the site is shown by maximum spring/summer concentrations of OH and HO_2 of 9×10^6 molecule cm^{-3} and 6×10^8 molecule cm^{-3}, respectively. After the primary photolysis source, the most important controls on the HO_x budget in this region are IO and BrO chemistry, the abundance of HCHO, and uptake of HO_x to aerosol.

Keywords Cape Verde · Trace gas · Saharan dust · Halogen chemistry · Dispersion model · Atlantic Ocean · Air-sea exchange

1 Introduction

It is well recognised that the tropics are of central importance for many aspects of the chemistry-climate system. High photochemical activity in tropical regions may acutely influence the lifetimes of certain greenhouse gases due to the intense oxidation chemistry occurring in this region. These regions profoundly influence the lifetime and concentrations of gases such as methane (Bloss et al. 2005; Lawrence et al. 2001) and ozone (Horowitz et al. 2003). The injection of tropospheric air into the stratosphere occurs predominantly within the tropics, and species which perturb the stratospheric ozone chemistry must first be processed through the tropics (Bridgeman et al. 2000). Ocean productivity in this region is also particularly sensitive to climate change: a prolonged decrease in net primary productivity of the low-latitude oceans over the last decade is linked to changes in upper-ocean temperature and stratification, which influences the availability of nutrients for phytoplankton growth (Behrenfeld et al. 2006; Richardson and Schoeman 2004).

Despite the crucial role played by the tropical atmosphere, it is under-populated with long-term observations compared to middle and high-latitudes. This paper describes the key scientific and technical features of the recently established Cape Verde Atmospheric Observatory Humberto Duarte Fonseca (CVAO) in the tropical eastern North Atlantic Ocean, including the site location, the instrumentation, and the chemical climatology and major signatures of the data collected so far.

Atmospheric processes in the eastern tropical North Atlantic are significantly influenced by long range transport and atmosphere-ocean exchange of trace chemicals. Cape Verde is located in a region of the Atlantic subject to sporadic but significant dust deposition originating in the African Sahara and Sahel regions. This dust transport has immediate impacts on humans, plus widespread influence on the radiative balance and on marine biological production and biogeochemical cycles. Mills et al. (2004) and references therein showed that community primary productivity in the tropical North Atlantic was nitrogen-limited, that nitrogen fixation was co-limited by iron and phosphorus and this could be stimulated by Saharan dust additions. Recently, Moore et al. (2009) showed that the iron supplied to the region by the large dust inputs controls the nitrogen fixation, which is globally significant. In addition, dust impacts on the ocean heat budget via the scattering of sunlight and reduction in surface solar insolation. As well as affecting the accuracy of some satellite temperature retrievals, dust outbreaks can lead to spatial gradients and significant variability in sea surface temperatures (Martínez Avellaneda et al. 2010). Indeed, aerosols exert their strongest influence on ocean temperatures in this region; ~ 35% of the observed changes in tropical North Atlantic Ocean summer surface temperatures has been attributed to trends in dust optical depth over the last 3 decades (Evan et al. 2009; Foltz and McPhaden 2008). In turn, the sensitivity of the dust/iron input to desertification and hydrological conditions in Africa (Prospero and Lamb 2003; Sokolik and Toon 1996) and atmospheric transport patterns (Moulin et al. 1997) suggests potential feedbacks between climate-forced changes in oceanic productivity, land-use and climate change.

The CVAO is downwind of the Mauritanian coastal upwelling region off northwest Africa, an area of high marine biological productivity. Observations made in Cape Verde therefore provide rare information on links between climate, marine biology and atmospheric composition changes. The productive marine biology in the region of Cape Verde may be at least partly responsible for the high levels of halogen oxides observed at the CVAO (Mahajan et al. 2010a; Read et al. 2008). These measurements have provided important observational evidence of the widespread impacts of halogen chemistry in the marine boundary layer, which had remained elusive until now. They show at least a regional effect of halogens on tropospheric ozone caused by the presence of pptv levels of IO and BrO, with halogens responsible for around 50% of the daily photochemical O_3 loss. Thus, these potentially major climate-related feedbacks involving (a) changes in cover and deposition of continental dust affecting marine ecosystems and the radiative balance and (b) alterations of ocean circulation, upwelling and marine biological production and consequent changes in oceanic gas emissions, can be studied very effectively in the vicinity of Cape Verde.

Here we characterise the air masses arriving at Cape Verde according to their origin and trajectories using the UK Meteorological Office NAME dispersion model (Ryall et al. 2001). We evaluate how these different air masses influence the chemical properties of air in this region, describe the seasonality of gas phase and aerosol composition and the intense photochemical cycling at Cape Verde, and evaluate the performance of a dust model for capturing the wintertime dust events in the region.

2 Site and sampling descriptions

2.1 Site description

The CVAO is located on a north-east facing lava field at Calhau on the island of São Vicente (16° 51′ 49 N, 24° 52′ 02 W), 50 m from the coastline and 10 m above sea level, with the north-easterly prevailing trade winds blowing directly off the ocean (Fig. 1). The Cape Verde archipelago is volcanic in origin and the islands shelve steeply to the deep abyssal plain beyond the African continental shelf. There are no obvious major coastal features such as extensive shallows or large seaweed beds. Such a site offers a rare opportunity for ground-based studies of clean marine air.

The origins of air drawn in to the trade winds arriving at Cape Verde are diverse; from North America, the Atlantic, Arctic, European and African regions. During late spring and summer, the site mostly receives North Atlantic marine air along the NNE trade winds with an African coastal influence, allowing the long-term study of "background" Atlantic air frequently influenced by the Mauritanian upwelling and its associated oceanic gases. During autumn and winter, Cape Verde is situated in the direct transport pathway of westerly dust from Africa to the North Atlantic. Section 3.1 discusses the air mass histories and trajectories in detail.

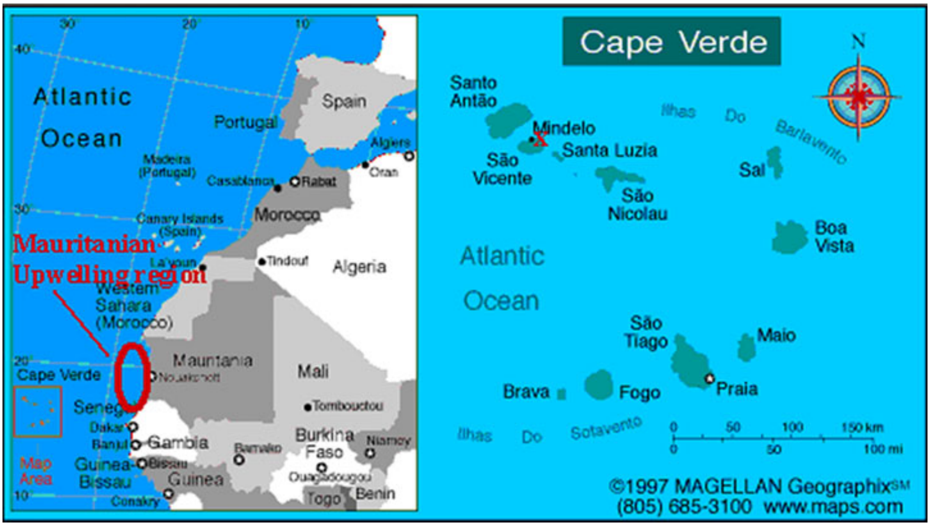

Fig. 1 The Cape Verde Islands and location of the Observatory, marked on São Vicente with a red cross. The Mauritanian upwelling region is marked in red. Prevailing trade winds are from the north-east

2.2 Infrastructure

Containerised laboratories form the main infrastructure of the CVAO, one each to house the trace gas measurements, greenhouse gas measurements and aerosol measurements. The site is powered by mains electricity and, from 2009, a wind turbine which provides a peak power of 12 kW. Two back-up generators, wired in series, are triggered automatically at times of complete power-outs and during voltage drops. The generators are housed within a permanent shelter to protect them from the corrosive environmental conditions. There is also a concrete hut to house the main electrical boards and breakers for the site, and a toilet and shower which is supplied by a water tank and feeds a cesspit. There is no running water at the site. Due to the remote nature of the site internet connectivity is possible only through the use of either satellites (currently using the T11N satellite) or long distance 10 km relayed WiFi/radio link to the Instituto Nacional de Meteorologia e Geofísica (INMG) office in Mindelo. A 30 m wooden tower is used for the greenhouse gas inlet and for the mounting of equipment such as Hi-vol samplers, aerosol filtration instruments, radiometers and meteorological masts. Trace gas measurements of O_3, CO, nitrogen oxides (NO_x and NO_y), volatile organic compounds (VOCs), halocarbons, and additional meteorology measurements, are made from the top of a 10 m tower. A second O_3 measurement is concurrently made from a height of 4 m, with the instruments showing no statistically significant difference. A local site manager and technician perform day-to-day maintenance and trouble shooting, and instrument scientists make regular visits to the site.

2.3 Instrumentation

The CVAO is within a very small class of WMO-GAW long-term observing stations that measure a comprehensive range of atmospheric parameters. These include meteorological parameters, greenhouse gases, short-lived reactive gas species and aerosols. Table 1 gives details of the instrumentation and their performance, and the data coverage for each

Table 1 CVAO instruments, their performance and data coverage

Measurement Species	Instrument	Performance	Timescale of measurements	Responsible Institution
Permanent Measurements				
Meteorological data at 4 m, 10 m and 30 m	Automatic Weather Station		Oct 06 - present	NCAS, University of York, UK
Solar radiation	Spectral Radiometer	280 ->950 nm (UV and VIS-Band)	Apr 08-present	Institut für Meereskunde, Hamburg, Germany
JO^1D	Radiometer	1 min integration time	Jan - Feb 07, May -Jun 07, Apr 08 - present	University of Leeds, UK NCAS, University of York, UK
Ozone	UV Absorption TEI 49 C and 49i	1 min integration time, 1 ppbv detection limit (dl)	Oct 06 - present	NCAS, University of York, UK
Carbon Monoxide	VUV Fluorescence, Aerolaser 5001	1 min integration time, 2 ppbv dl	Oct 06 - present	NCAS, University of York, UK
NO, NO_2, NO_y	Chemiluminescence, Air Quality Design Inc	1 h integration time, 1.5, 4, 3 pptv dl for NO, NO_2, NO_y respectively	Oct 06 - present	NCAS, University of York, UK
Speciated NOy - ∑PANs, nitrate aerosol, ∑alkyl nitrates	Heated quartz inlets-Chemiluminescence	1 h integration time, ~10 pptv dl	Apr 09 - present	NCAS, University of York, UK
C_2-C_8 NMVOCs and DMS	Dual channel GC-FID	1 h integration time, 2.5, 1 pptv dl for C_2-C_4 and > C_4 respectively	Oct 06 - present	NCAS, University of York, UK
Methanol, acetone, acetaldehyde	Dual channel GC-FID	1 h integration time, 3, 7, 18, pptv dl for acetone, methanol and acetaldehyde and respectively	Oct 06 - present	NCAS, University of York, UK
Halocarbons	GC-MS	30 min integration time, 0.05 pptv dl	May 07, Sep 07-Jan 08, Sept 09-May 10	University of Bristol, UK until 2011; Universities of York and Bristol from 2011

Table 1 (continued)

Measurement Species	Instrument	Performance	Timescale of measurements	Responsible Institution
Chemical characterisation of aerosol PM_{10}, Mg^{2+} Ca^{2+}, NH_4^+, Na^+, K^+, Br^-, Cl^-, NO_3^-, SO_4^{2-}, OC, EC, oxalate and in campaigns other dicarboxylic acids, organic compounds, metals (Ti, Mn, Fe, Ni, Cu, Zn) in five size fractions	HiVOL Sampler, Digitel DHA-80 Subsequent analysis Ion chromatography, thermographic methods, CE-MS, and GC-MS, 5 stage Berner Impactor, size segregated analysis, TXRF for metal analysis	1, 1, 1, 1, 2, 2, 1, 5, 8, 9, 3, 5 ng m^{-3} dl	Nov 06-present only during campaigns (1–2 month per year)	Leibniz-Institut für Troposphärenforschung, Germany
Physical characterisation of Aerosol Size distribution (12 nm–10 μm) and number concentration	SMPS (10–800 nm), APS (0.6–10 μm).	15 min sampling	May 07-present	Leibniz-Institut für Troposphärenforschung, Germany
Aerosol Absorption 300–800 nm	MAAP	1 h	June 08- present	Leibniz-Institut für Troposphärenforschung, Germany
CH_4, CO_2, N_2O, CO, SF_6, ratio of O_2/N_2, and Ar/N_2 isotope ratios of $^{13}C/^{12}C$ and $^{18}O/^{16}O$ of CO_2 and O_2	Flask sampling	0.7, 30, 0.3, 1.4 ppbv dl for CH_4, CO_2, N_2O, CO respectively	Jan 07-present	Max-Planck-Institut für Biogeochemie, Jena, Germany
O_2, N_2, SF_6, CH_4, N_2O	Gas Chromatograph	12 min integration time, Detection limits: CH_4: 1 ppbv CO: 0.5–1 ppbv SF_6: 0.05–0.1 pptv N_2O: 0.1–0.2 ppbv	June 08-present	Max-Planck-Institut für Biogeochemie, Jena, Germany
CO_2	NDIR	12 min integration time, 0.005 ppmv dl	June 08-present	Max-Planck-Institut für Biogeochemie, Jena, Germany

Table 1 (continued)

Measurement Species	Instrument	Performance	Timescale of measurements	Responsible Institution
O_2	O_2 Paramagnetic instrument	16 min integration time, 2–3 per meg dl	Jun 08-present	Max-Planck-Institut für Biogeochemie, Jena, Germany
$BrO/IO/NO_2/O_4$	MAX-DOAS	IO, 1.5 pptv BrO, 4.4 pptv NO_2 150 pptv	Nov 06–Jan 08, Sep 08–May 09, Nov 09 - present	Institute of Environmental University of Heidelberg, Germany
PM_{10} high volume 720 m³/day	DIGITEL DHA-80 HV-sampler	24 (48) hour sampling interval	May-Jun 07, Dec 07, Jul 08, Jan-Feb 09, May-Jun 09, Jan-Feb 10, Jan-Feb 11	Leibniz-Institut für Troposphärenforschung, Germany
Size segregated PM (50 nm–40 nm–420 nm–1.2 µm–3.5 µm–10 µm)	Berner Impactor	24 (48) hour sampling interval	May-Jun 07, Dec 07, Jul 08, Jan-Feb 09, May-Jun 09, Jan-Feb 10, Jan-Feb 11	Leibniz-Institut für Troposphärenforschung, Germany
Hygrsocipicity measurements	Humidified DMA-APS to distinguish between seasalt and mineral dust	20 min	May 07 - present	Leibniz-Institut für Troposphärenforschung, Germany
Aerosol Absorption 300–800 nm	SOAP	1 h	May 07 - present	Leibniz-Institut für Troposphärenforschung, Germany
Non-permanent measurements				
$BrO/IO/I_2$, OIO	LP-DOAS	20 min integration time, 0.9, 0.5, 5, 2 pptv dl	Nov 06-Jun 07, Feb-Nov 09	University of Leeds, UK
$BrO/IO/O_3/NO_2/I_2/OIO/HONO/HCHO/ClO/NO_3/Glyoxal$	LP-DOAS (up to 4 light paths)	single sample time 1 min, full run 4 light paths 25 min; dl: 0.8/0.6/1000/30/8/2/40/300/30/2/70 pptv	Jun 10 – Oct 10 (June and Oct measurements on 4 light paths)	University of Heidelberg, Germany
$IO/NO_2/Glyoxal$	CE-DOAS	5 min, dl: 0.8/2/120 pptv	Jun 10	University of Heidelberg, Germany

Table 1 (continued)

Measurement Species	Instrument	Performance	Timescale of measurements	Responsible Institution
Cloud base	Ceilometer	Up to 25 000 ft Acquisition time minimum 15s, maximum 120s	Aug 07–Jun 08	NCAS, University of York, UK and IFM-GEOMAR (Leibniz-Institut für Meereswissenschaften an der Universitat Kiel)
Leachable metals, NO_3, PO_4, DON, DOC, total metal and P conc.	4×47 mm filters, ICP-MS, high temperature combustion TOC-TDN ion chromatography and nutrient analysers	48–72 h sampling	July 07–October 09	National Oceanography Centre, Southampton, UK
Dornier Aircraft measurements of O_3, CO, VOCs, aerosol	Various	10 s integration time; 1ppbv, 2ppbv, 1 pptv, dl for O_3, CO, VOCs respectively	May 07, Sept 09	NCAS, University of York, UK
During RHaMBLe 4-week (18th May–15th June 2007) Intensive Experiment				
OH, HO_2	FAGE-LIF	0.04 (OH), 0.05 (HO_2) pptv dl (1 min)	May-Jun 07	University of Leeds, UK
Cl_2, I_2, Br_2	Atmospheric Pressure Chemical Ionization Tandem Mass Spectrometry	1 h integration time, 1.9, <0.2 and <0.3 pptv dl for Cl_2, I_2 and Br_2 respectively	May-Jun 07	University of California, Irvine, USA
HCl, Cl* (HOCl + Cl_2), HNO_3, HCOOH, CH_3COOH, HONO	Tandem mist chambers/Ion chromatographs	2 h integration time, 26, 14, 12, 29, 44 pptv dl for HCl, Cl^*, HNO_3, HCOOH, CH_3COOH respectively	May-Jun 07	University of Virginia and University of New Hampshire, USA
Total volatile inorganic Br and I	Filter pack, neutron activation analysis	4.9 and 2.7 ng m^{-3}	May-Jun 07	University of Virginia and University of New Hampshire, USA
Halocarbons	GC- ECD	<1 pptv dl	Jun 07-Jul 07	University of Cambridge, UK

Table 1 (continued)

Measurement Species	Instrument	Performance	Timescale of measurements	Responsible Institution
During Seasonal Oxidant Study 4×3 week campaigns 2009				
OH, HO_2	FAGE-LIF	0.04 (OH), 0.05 (HO_2) pptv dl (1 min)	Feb, May, Sept, Nov 09	University of Leeds, UK
HO_2, RO_2	PERCA	10 min integration time, 0.04 pptv dl and 38% error	Feb, May, Sept, Nov 09	University of Leicester, UK
Photolysis rates	Radiometers	1 min integration time	Feb-Nov 09	University of Leicester, UK
Dihalogens, HOCl/HOBr	Quadrapole Mass Spectrometry	1 h integration time, 1.9, <0.2 and <0.3 pptv dl for Cl_2, I_2 and Br_2 respectively	May-Jun 09	University of California, Irvine, USA

measurement. Most measurements at the ground-based observatory began in October 2006, with others phased in after that date. Details are also given of measurements made during the "Reactive Halogens in the Marine Boundary Layer" (RHaMBLe; 18th May–15th June 2007, (Lee et al. 2010)) and the Seasonal Oxidant Study (SOS; 3 separate intensives in 2009) intensive field campaigns.

2.4 Meteorology

Temperature, relative humidity, and wind measurements were collected from 30 m and from 10 m at 1 Hz then averaged over 1 minute and 10 minutes. Atmospheric pressure and broadband UV radiation were recorded at 4 m. Cloud base height was estimated from continuous laser ceilometer (Vaisala, CL31) data, and boundary layer height from radiosonde profiles deployed from the island of Sal (http://esrl.noaa.gov/raobs/). $J(O^1D)$ was measured at 4 m with a 2π filter radiometer (Meteorology Consult Gmbh) with <5% precision and ~20% accuracy for solar zenith angles (SZA) below 60°, and corrections were applied for the vertical overhead O_3 column and changes in sensitivity due to changing SZA.

2.5 Reactive trace gases

Ozone is measured every minute from a height of 4 m and 10 m using UV absorption instruments (Models 49C and 49i Thermo Scientific). The instruments give an absolute measurement of ozone with a precision of 0.07 ppbv for hourly averaged data. CO mixing ratios from 10 m are determined using an Aerolaser 5001 fast response VUV analyser, with a detection limit of <0.5 ppbv on 1 minute average. Measurements of NO_x are made from 5 m using a single channel, chemiluminescence NO detector with a photolytic NO_2 converter (Lee et al. 2009). The instrument (Air Quality Design Inc) alternates between measuring NO, NO_2, total NO_y, PANs and alkyl nitrates in a 10 minutes duty cycle, with hourly averaged data giving detection limits of 1.5 pptv and 4 pptv for NO and NO_2, respectively. Total NO_y is measured by molybdenum catalytic conversion to NO, followed by chemiluminescence detection. PANs and alkyl nitrates are measured by thermal decomposition to NO_2 on a quartz surface at 150°C and 350°C, respectively (Farmer et al. 2006). The NO_2 is then photolytically converted to NO with subsequent chemiluminescence detection.

Hourly VOC and OVOC measurements (C_2–C_8 NMHC, dimethyl sulphide and C_1-C_3 OVOC) are made from 10 m using a dual-channel gas chromatograph with flame ionisation detection (GC-FID) (Hopkins et al. 2003; Read et al. 2009). Detection limits for VOCs ranged between 2–10 pptv. Weekly CH_4 measurements were obtained using flask samples with subsequent gas chromatographic analysis.

Peroxy radical ($HO_2 + RO_2$) measurements made using the PERCA technique ((Fleming et al. 2006) and references therein) were conducted as part of the Seasonal Oxidant Study (SOS) which covered three intensive measurement periods (27/02/2009 to 15/03/2009 (SOS 1), 20/05/2009 to 02/06/2009 (SOS 2) and 02/09/2009 to 14/09/2009 (SOS 3)). OH and HO_2 (HO_x) were detected by Laser-Induced Fluorescence spectroscopy using two FAGE (Fluorescence Assay by Gas Expansion) instruments (Heard and Pilling 2003). A ground-based FAGE was deployed during the RHaMBLe experiment May-June 2007 (Whalley et al. 2010) and an aircraft instrument (Commane et al. 2010; Vaughan et al. 2011) was stationed at the observatory from February to December 2009, and made measurements in its ground configuration during the three intensive SOS periods, as described in Table 1.

Mixing ratios of halogen species (IO, BrO, OIO and I_2), nitrate (NO_3), formaldehyde (HCHO) and glyoxal (CHOCHO) were retrieved from long-path differential optical absorption spectroscopy (LP-DOAS) using the University of Leeds (UOL) LP-DOAS instrument (Plane and Saiz-Lopez 2006). The LP-DOAS instrument comprised a Newtonian telescope acting as a transmitter and receiver, and an array of retro-reflectors placed 6.1 km across a bay from the observatory (resulting in a total optical path length of 12.2 km). Spectra were collected every 30 s and then further averaged over 20–30 min to improve the signal-to-noise ratio, resulting in detection limits of 0.5 pptv for IO, 0.9 pptv for BrO and 170 pptv for HCHO. Detection limits of 15 pptv for I_2, 10 pptv for OIO, 4 pptv for NO_3 and 150 pptv for CHOCHO were estimated. The LP-DOAS instrument was based at Cape Verde for two periods; first during November 2006–June 2007, and second during October 2008–August 2009. In addition to the LP-DOAS, a Multi-Axis Differential Optical Absorption Spectroscopy (MAX-DOAS) instrument from the University of Heidelberg (UOH) has run near continuously since November 2006. It contains a moveable telescope device with an integrated spectrometer which collects scattered sunlight from discrete elevation angles between 2° and 40°, and in the zenith. The instrument measures the integrated concentration of species (SCD) along different lines of sight. The SCD are used to model the vertical distribution and concentration of the species (Deutschmann et al. 2011). The integration time for each of the seven measured elevation angles is 2 min which results in a total temporal resolution of 14 min and a detection limit of 4.4 pptv for BrO, 1.5 pptv for IO and 150 pptv for NO_2. From June to October 2010 additional LP-DOAS and in June 2010 also Cavity Enhanced (CE)—DOAS measurements were performed by the UOH. The applied LP-DOAS is a new fibre optic setup (Merten et al. 2011) which has a higher light throughput and thus allows a shorter total spectral sampling time of 1 min. The instrument measures successively all wavelength ranges from 270 nm up to 680 nm and thus all relevant trace gases continuously. The absorption path for the measurements from June to October is the same as that from UOL, with the reflector placed 6.1 km across the bay. As the instrument can automatically switch between different absorption light paths, during intensive field campaigns in June and October, additional measurements across half of the bay (2.8 km) to reflectors at different heights (0 m, 45 m, 92 m, 560 m) were performed to retrieve the vertical profile of the trace gases. The total measurement time using all reflectors and at all wavelengths was about 25 min. The resulting detection limits for the long absorption path are 0.6 pptv for IO, 0.8 pptv for BrO, 1 ppbv for O_3, 30 pptv for NO_2 and 300 pptv for HCHO. The CE-DOAS is a broad band absorption cavity working in the spectral range from 430 nm to 460 nm and derives in situ trace gas concentrations of IO, NO_2 and glyoxal ($C_2H_2O_2$). The instrument was set-up at CVAO, and during one day directly at the water front. Due to the high aerosol load from sea spray the detection limit is relatively high with 2 pptv for IO (5 min resolution) and 1.5 ppt (50 min resolution).

2.6 Greenhouse gases (CO_2, CH_4, CO, N_2O, SF_6) and oxygen

The automated greenhouse gas measurement system integrates a Paramagnetic O_2 analyser (Servomex Company Inc, PM1155), NDIR CO_2 analyser (Siemens AG, Ultramat 6 F) and a Gas Chromatograph (GC, Agilent Technologies, 6890A) with a Flame Ionization Detector (FID) used for CH_4 and CO measurements and an Electron Capture Detector (ECD) for N_2O and SF_6 measurements. The measurement system occupies a contained air-conditioned laboratory with temperature typically stable to ±0.2–0.5°C. A suite of calibration gas cylinders are kept horizontally in a thermally insulated enclosure (Blue Box) and shared between all the analysers. The details on the system's setup, operation, calibration and data quality control have been presented elsewhere (Kozlova and Manning 2009). The measurement system provides concentration data on a semi-continuous basis (one air measurement every 16 and 12 min for O_2 and CO_2 and for the GC species, respectively). The measurement system was installed in May 2008 and has been in operation (with periods of down time due to several technical problems) since October 2008. In addition to the continuous air measurements, flask samples have been collected mostly bi-weekly since March 2007. The flasks are shipped back to MPI-BGC where the air is subsequently analysed for CH_4, CO, N_2O and SF_6 concentrations, O_2/N_2 and Ar/N_2 ratios, and isotopic composition of CO_2 ($\delta^{13}C\text{-}CO_2$). The air inlets for both the continuous measurement system (inlets for O_2 and CO_2, and the GC species are separate) and the flask sampling unit are installed at 30 m (top of the tower), next to each other. An aspirated inlet has been installed on the O_2 and CO_2 sampling line to minimise the fractionation at the air intake (Blaine et al. 2006).

2.7 Aerosol sampling, chemical and physical characterization

2.7.1 Aerosol sampling

Aerosol is sampled at the top of a 30 m high tower to avoid the influence of surf-produced sea spray aerosol. IfT-Leipzig sample continuously (since January 2007) using a high volume (HV) sampler equipped with a PM_{10} inlet (DHA-80, Digitel Elektronik AG, Switzerland), with samples collected on pre-heated quartz fiber filters (110°C for 24 h, 150 mm Munktell, Sweden) at a flow rate of 500 $L min^{-1}$. In addition, size-segregated aerosol samples were collected during six intensive campaigns (17th May–14th June 2007, 28th November 2007–5th January 2008, 28th June–1st August 2008, 7th January–15th February 2009, 14th May–10th June 2009, and January–February 2010) using a five stage Berner-type impactor with 50% cut-off sizes at 0.05, 0.14, 0.42, 1.2, 3.5 and 10 μm. The particles were collected on pre-heated aluminum foils (300°C, 3 h) at a flow rate of 75 $L min^{-1}$. For the metal analysis, a piece of Nuclepore polycarbonate foil was added on the aluminum foil (Wicom, Germany). During intensive campaigns the sampling time for filter and impactor samples was typically 24 h. During other times impactor samples were not taken and the filter samples were taken over 72 h. The samples were stored at −20°C until analysis.

The National Oceanography Centre Southampton collected aerosol dust from the top of the 30 m tower using a low volume aerosol sampler in the period between July 2007 and October 2009. Samples were collected simultaneously onto four 47 mm 0.4 μm pore-size membrane filters; two polycarbonate filters (Nuclepore) and two polypropylene filters (Sterlitech). Mass flow meters were used to measure the volume of air sampled through each filter. The filters were changed three times per week. Typical flow rates were 20–30 $L min^{-1}$ per filter, giving total sample volumes of 50–100 m^3. Samples were stored frozen (−20°C) until analysis in the UK, as aerosol solubility has been reported to decrease when samples are stored at room temperature (Buck et al. 2006).

2.7.2 Chemical aerosol analysis

Particle mass and total organic carbon content (TOC) were determined from the HV and Berner samples (Müller et al. 2009; Müller et al. 2010). Also, the non-purgeable organic carbon content (NPOC) was measured from the HV samples using a TOC-V CPH system

(Shimadzu, Kyoto, Japan). Single compound analyses were done from the Digitel and Berner samples for more detailed aerosol characterization. The ions were determined from an aqueous filter extract using standard ion chromatography (IC) (Metrohm 690 and 761 Compact IC, Switzerland) (Müller et al. 2010). The organic anions including methanesulfonic acid (MSA) and smaller dicarboxylic acids were determined from an aqueous filter extract using capillary electrophoresis with UV-detection (CE-DAD) (Spectra Phoresis 1000, Thermo Separation Products, USA). Low molecular weight aliphatic amines were also determined from the aerosol samples. The amines were determined after a derivatization step using high performance liquid chromatography coupled to an electrospray ionization ion trap mass spectrometer (HPLC/ESI-ITMS) (Müller et al. 2009). In addition, the metal composition was characterized from the size segregated aerosol samples using total reflection X-ray fluorescence spectrometry (TXRF, Bruker AXS, Germany) (Müller et al. 2010).

The low volume samples were used to investigate the solubility of the aerosol dust constituent trace metals and nutrients (NO_3^-, NH_4^+ and PO_4^{3-}, dissolved organic carbon (DOC), dissolved organic nitrogen (DON), total chemical composition and mineralogy. Total chemical composition of the dust was investigated by total acid digestion of the polycarbonate filters followed by Inductively Coupled Plasma Mass Spectrometry (ICP-MS) analysis for a broad suite of metals. A simple ultrapure water leach was used with the polypropylene filters to investigate the readily soluble fraction of metals and nutrients in the samples. For this procedure,100 ml of ultrapure water was passed through the filter using a filtration apparatus and a small vacuum pump (Buck et al. 2006). The resulting filtrate was analysed for nutrients (NO_3^-, NH_4^+, PO_4^{3-}) using a standard nutrient autoanalyser, anions ($Cl^-$and SO_4^{2-}) using ion chromatography, DOC, DON using a high temperature combustion TOC-TDN analyser (TOC-V-CPN, Shimadzu), and a broad suite of metals using an ICP-MS (X-series, Thermo). The filtrations were completed within 10 s, and hence were akin to a chromatographic process whereby fresh eluent is passed over a stationary phase consisting of the aerosol material (Buck et al. 2006). The Fe concentrations in the leachates (ca. pH 5) were typically below 1 μM, but for some samples the thermodynamic $Fe(OH)_3$ saturation concentrations may have been briefly exceeded whilst the ultrapure water was in the aerosol layer on the filter. However, with the relatively slow water exchange rate constant for Fe^{3+} (200 s^{-1}) (Morel and Hering 1993) and the rapid filtration procedure, we consider the Fe saturation of the leachate in the aerosol layer to constitute a minor potential loss factor.

2.7.3 Physical Aerosol measurements

Continuous measurements of particle number size distribution (PNSD), sampled from 30 m, have been made since July 2008. Prior to May 2007, aerosol was measured 4 m above ground and was highly influenced by sea spray; these measurements are not discussed here. A 30 m stainless steel tube with a ¾" outer diameter leads from the tower to an air conditioned container housing the measurement equipment. A PM 10 inlet dimensioned for a flow rate of 16.6 $l min^{-1}$ is installed on top of the stainless steel tube. Sample air is dried to a relative humidity less than 40% by a self constructed aerosol dryer (Tuch et al. 2009) before reaching the aerosol instrumentation. Aerosol losses in the tubes were corrected according to Baron and Willeke (2001) and the correction of losses in the dryer followed Tuch et al. (2009).

The measurements in the size range of 0.01–0.8 μm were conducted with a Scanning Mobility Particle Sizer (SMPS) (Wang and Flagan 1989). In parallel, an APS (TSI 3320, TSI Inc., St. Paul Minnesota, USA) was used to measure the aerodynamic size distribution in the size range of 0.6–10 μm. To combine both size distributions, a density and a shape factor depending on ambient conditions (dust or pure sea salt) were assumed and the aerodynamic diameters were converted to volume equivalent diameters (DeCarlo et al. 2004). Furthermore, volume and surface concentration as well as volume and surface size distributions can be extracted from the measurements, which is especially relevant for radiation information.

2.8 Dust modeling

Satellite remote sensing is useful to characterize the spatiotemporal distribution of the Saharan dust plume and has also been used to estimate dust fluxes into the North Atlantic (Kaufman et al. 2005). However, a better understanding of the oceanic dust deposition processes including information about the origin of the dust aerosol and atmospheric processing is obtained from atmospheric dust transport models (e.g. Mahowald et al. (2005))). Global-scale dust models can provide information about averages and spatiotemporal variability of dust transport and deposition patterns, where differences between different models indicate uncertainties in the parameterization of emission and deposition processes as well as deficiencies in reproducing transport patterns (Huneeus et al. 2011). In contrast, regional scale models are particularly suitable to investigate Saharan dust transport for specific meteorological situations.

Here we use the regional model system COSMO-MUSCAT to describe the input of Saharan dust into the tropical Atlantic (Heinold et al. 2007; Schepanski et al. 2009; Heinold et al. 2011), using aerosol observations from the CVAO for model validation. The model system consists of the mesoscale meteorological model COSMO of the German Weather Service (Deutscher Wetterdienst, DWD) and the MUltiScale Chemistry Aerosol Transport Model (MUSCAT). For this application the domain includes the major part of the Sahara desert and extends to the Cape Verde islands, and the model operates with 28 km horizontal grid resolution and 40 vertical layers. Dust emission, transport, and deposition are simulated using meteorological and hydrological fields from the meteorological model, including the computation of the direct dust radiative effect on atmospheric dynamics. Dust emission fluxes cannot be observed directly, but are computed from simulated meteorological fields and compiled information on surface properties (vegetation cover, surface roughness, soil texture). The location of potential dust sources derived from Meteosat Second Generation satellite observations are taken into account for dust emission calculations. The simulated dust is transported as a passive tracer in several independent size classes between 0.1 μm and 25 μm radius. The model removes dust particles from the atmosphere by dry and wet deposition processes. Dry deposition (gravitational settling and turbulent mixing) depends on particle size, density and relevant meteorological parameters. The parameterization of wet deposition accounts for rain-out and wash-out. Dust particles removed from the atmosphere are then available at the ocean surface.

2.9 QA/QC and Data management

Data are supplied to the British Atmospheric Data Centre (BADC) on a monthly basis for O_3, CO, NO, NO_2, and meteorological data, or, for those data requiring extensive post processing (i.e. VOCs, o-VOCs, halocarbons, aerosol data), within 1 year of collection. Data are available immediately for public dissemination from the Data Centres upon registration.

In 2008 the site was accepted as a Global Atmospheric Watch (GAW)-contributing station for the gas phase species and was upgraded to a Global station in August 2009. Hourly data for carbon monoxide, ozone, NO_x and NO_y are submitted to the World Data Centre for Greenhouse Gases (WDGCC) (as well as to BADC) with measurements of VOCs and greenhouse gases to follow. In addition, the site is one of only a few existing stations which make long-term VOC measurements and as a result is integral in the set-up of the newly established GAW VOC network.

Calibrations for O_3, CO and NMHCs are linked to the recognized GAW primary standards via the relevant Quality Assurance Science Activity Centre (QA/SAC) established by GAW. The QA/SAC provides support for the local quality assurance (QA) system under the guidelines and recommendations of the GAW Scientific Advisory Groups. Other parameters are calibrated as described in section 2.3.

3 Results

3.1 Dispersion modelling of air mass history and their classification

The UK Meteorological Office NAME dispersion model (Ryall et al. 2001) was used in passive tracer mode to study the origin and pathways of inert tracers (particles) arriving at the station's coordinates between October 2006 and September 2009. The model was run with Unified Model (UM) global meteorological data (40 km resolution). Ten-day air mass history footprints were calculated for three hourly periods and these have been integrated into monthly footprints as shown in Fig. 2 for 2008.

Seasonal changes in the air masses that influence the Cape Verde islands are evident, with a much greater influence of the Saharan region in the winter months (particularly December to February) and a greater number of trajectories originating from the Arctic and Europe in the spring and summer. Much of the seasonal variation in the air mass origins can be attributed to the changing location and structure of the subtropical "Azores" high pressure system which resides to the north of Cape Verde. In the climatological mean (based on NCEP/NCAR 1948–2010 re-analysis (Kalnay et al. 1996), during the summer, the high pressure system is typically restricted to the central Atlantic ocean where it forms a coherent region of descent and anti-cyclonic flow. Thus in these months the air flow is generally from the north-east. This leads to flow along the European and African coast as shown by the trajectories. In the winter months the high pressure system extends over a much larger region from the Caribbean to the Middle East. In this situation the air flow to Cape Verde has a more significant African component. Again the trajectory analysis reflects this general change in the large-scale meteorology.

The 2007 and 2009 monthly-integrated footprints show a similar seasonality to the year 2008, with small differences in the intensity and influence of the Saharan area. For example, in December 2006 and 2007, the footprints extend further eastward into the Saharan region than in winter 2008/2009. This can be seen in the smaller Saharan influence in winter 2008/2009 in Fig. 4 as discussed later.

The predominant wind direction of air masses in the last few hours before arriving at the site is from the north-east; this is almost exclusively the case during the summer months (June to October). Note that there are practically no air masses arriving from a southerly direction.

We have defined the area around the site into 5 broad regions of influence, as shown in Fig. 3 by assigning each 5° x 5° box in the domain of interest to a region.

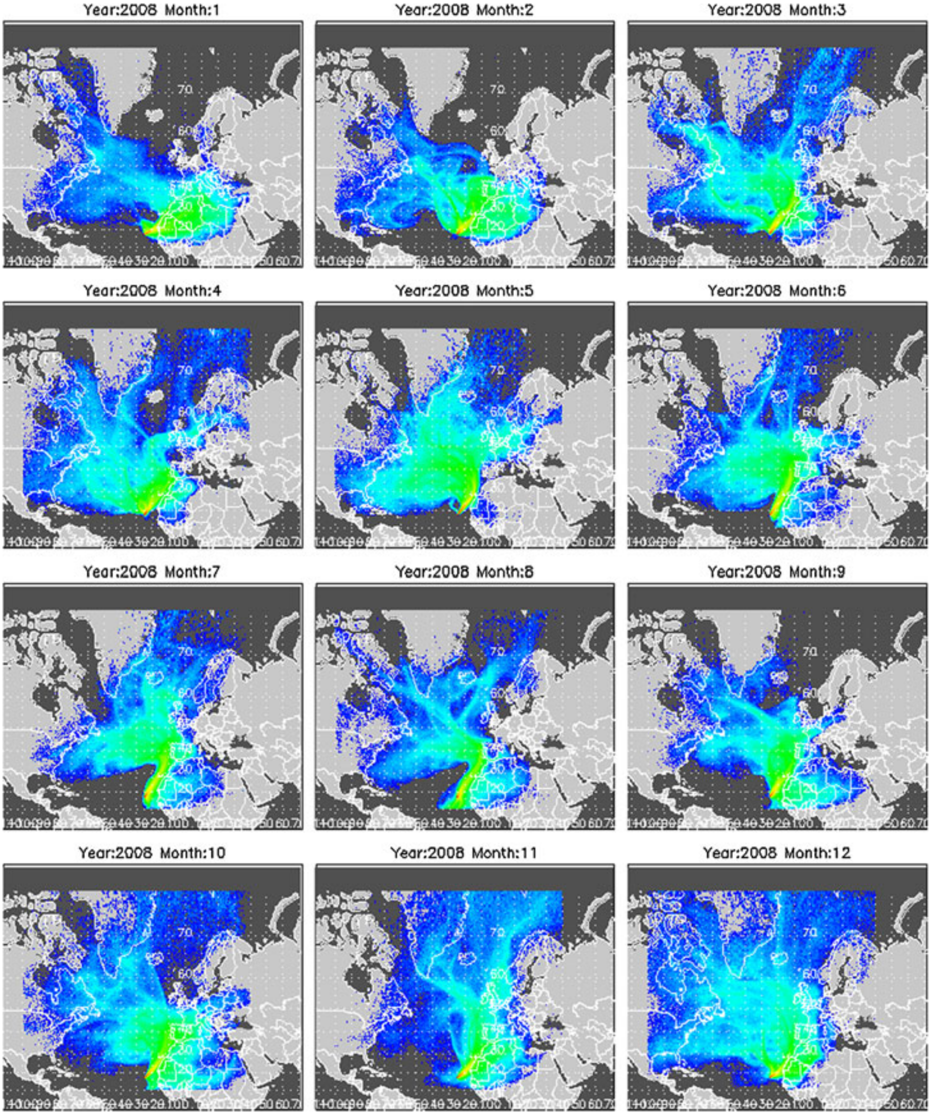

Fig. 2 2008 monthly integrated NAME footprints for CVAO, consisting of accumulated 3 h releases for 10 days backwards

These regions, which are similar to the air mass categories defined in Lawler et al. (2009) and Lee et al. (2009) are:

(i) Coastal African: Nearly all air masses pass over the coast of northwest Africa and hence the Mauritanian upwelling (Hagen 2001) before reaching the site
(ii) Polluted Marine: Air masses passing over Europe, particularly the Iberian peninsula
(iii) Saharan Africa: Dust, with influence from cities in Mauritania (Noaukchott) and Senegal (Dakar).
(iv) Atlantic: Further delineated into trajectories originating over the Atlantic (Atlantic marine) and over North America (Atlantic continental) during the previous 10 days

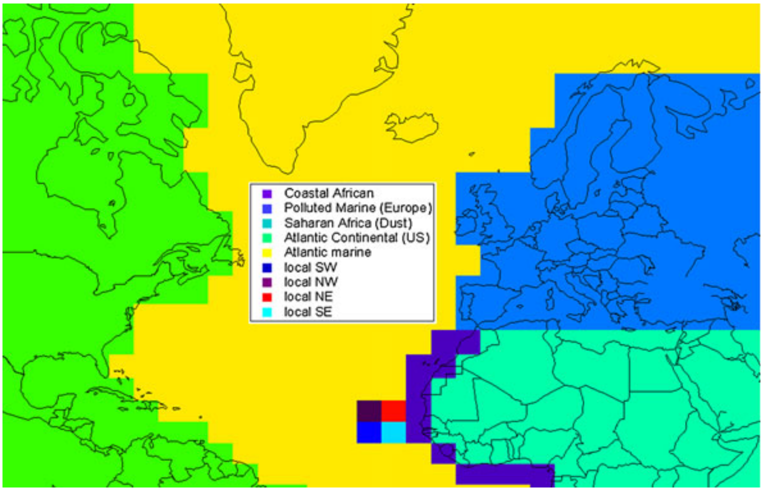

Fig. 3 Geographical sector divisions for classification of the land and marine footprints influencing Cape Verde

Finally, the four 5×5 grid boxes surrounding the station were allocated to assign the local wind direction and to create a record of local influences due to air arriving outside of the NE sector or to very low wind speed conditions during NE winds. Less than 5% of air masses arrived from the SW and SE sectors. If the amount of particles originating from the NE 5×5 grid was over 30% of the total during the 10 day passageway (signifying low wind speeds) then this time stamp was also assigned a local flag (which occurred 19% of the time). The local index occurs more frequently in winter (September-February).

The model was run to capture any air masses arriving at the station in the lowest 100 m (ground level and in the boundary layer), so that any emissions released from the surface would be picked up by this air mass. From the 5×5 grid divisions for each region in Fig. 3, the percentage of particles passing over each of the five main sectors was calculated for every 3 hourly NAME footprint from October 2006 to September 2009.

All trajectories in their ten-day journey pass over a combination of these sectors as shown by the time series of regional influences on Cape Verde during 2007–2009 shown in Fig. 4. Note the seasonality of the Saharan air mass in particular, with a much greater presence in winter and a very small influence in the summer months; this is also clear from the monthly footprints shown in Fig. 2.

Air mass trajectory classifications for each 3-hour trajectory arriving at Cape Verde were assigned according to their time spent over the 5 geographical sectors shown in Fig. 3. First a threshold, relating to the number of particles arriving from each sector, was defined in order to assess which sectors were significantly influencing each 3-hour period. In order to avoid bias in favour of the sectors that experience the greatest number of particles passing over them (i.e. the Atlantic and African sectors), this threshold was calculated as 10% of the sector's maximum concentration over the three years. The final threshold relative contribution for each sector were calculated as 12, 4, 9, 3 and 16% for coastal African, European, African, American and Atlantic sectors, respectively.

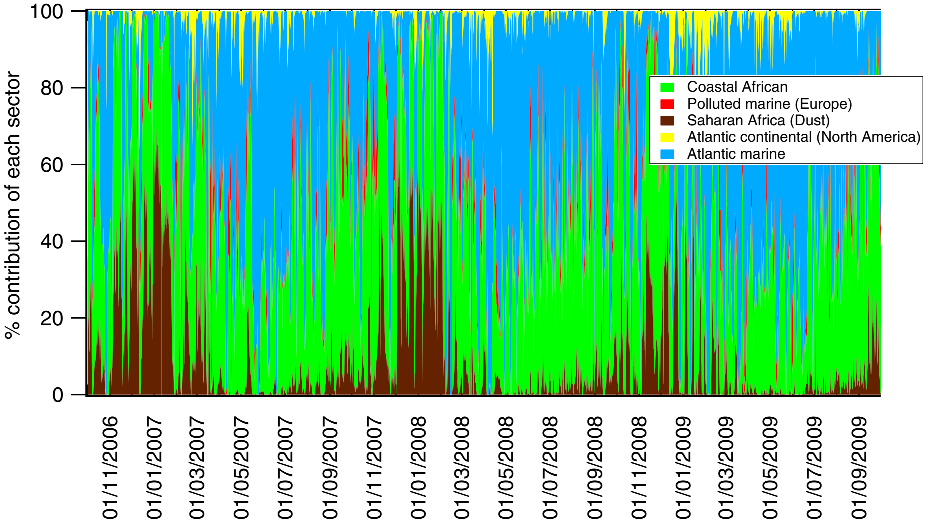

Fig. 4 Percentage contribution of the 5 main sectors to the number of particles (inert tracers) arriving at the station between October 2006 and September 2009 during 10 day back trajectories, as calculated by the NAME dispersion model

For each 3-hour period, the sectors of influence were used to classify each period into 7 trajectory types. The trajectories were defined as:

1) Atlantic and African coastal—AAC,
2) Atlantic marine—AM,
3) North American and Atlantic—NAA,
4) North American and coastal African—NCA,
5) European (with minimal African influence)—EUR,
6) African (with minimal European influence)—AFR,
7) European and African—EUR/AFR.

Example trajectories for this classification are shown in Fig. 5. These trajectory types were used to aid the analysis of differences in atmospheric composition, as discussed in section 3.6.

3.2 Boundary layer height, radiation, meteorological conditions

3.2.1 Boundary Layer height

The Atmospheric Boundary Layer (ABL) is defined as the part of the atmosphere directly influenced by the Earth's surface, often responding with a time scale of about one hour or less (Stull 1988). The ABL top is usually identified by a sharp increase in the potential temperature vertical profile (the inversion), and a decrease in humidity. Typical of the eastern sides of the Atlantic and Pacific in both hemispheres, air subsiding into the subtropical north-east Atlantic (in this case from further north and east) is warmer and drier than the air that has been in contact with the relatively cold ocean surface influenced by upwelling, and a strong inversion forms at the interface of the two air masses (Hanson

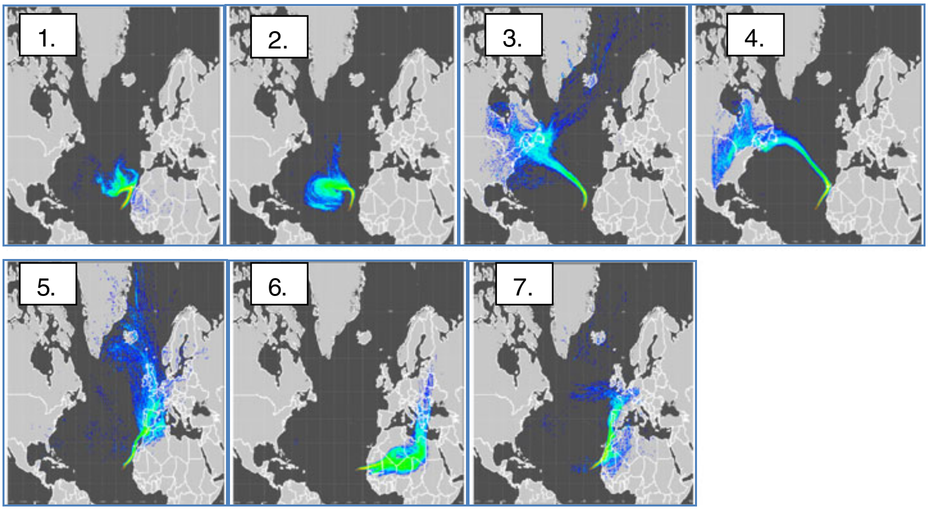

Fig. 5 Typical 10-day dispersion footprints of the 7 main air mass trajectories arriving at Cape Verde. 1) Atlantic and African coastal—AAC, 2) Atlantic marine—AM, 3) North American and Atlantic—NAA, 4) North American and coastal African—NCA, 5) European (with minimal African influence)—EUR, 6) African (with minimal European influence)—AFR, 7) European and African—EUR/AFR

1991). These conditions are favourable for the formation of marine stratocumulus cloud decks. In this region, the (relatively patchy) marine stratocumulus cloudiness tends to peak in July and August due to changes of position and intensity of the Northern Hemisphere subtropical highs (Hanson 1991). Hanson (1991) also noted that months with cooler than normal sea surface temperatures (SST) have more than normal cloudiness, suggesting that there may be a positive feedback between marine stratocumulus clouds and SST.

Here we define the depth of the ABL (h, corresponding to the stratocumulus cloud top), as where the vertical gradient of virtual potential temperature ($\partial\theta_v/\partial z$) first becomes greater than or equal to 3 $\mathrm{K\,km^{-1}}$ (Zeng et al. 2004). The potential temperature gradient was calculated from the NOAA ESRL radiosondes launched daily at 1200 (UTC) from the island of Sal, approximately 200 km from the Cape Verde Observatory. Figure 6a shows a typical vertical profile of θ and relative humidity (RH)—Note that the contrast between the surface air and the air above the inversion is substantial. The cloud layer is taken as the layer where the relative humidity is larger than 90%—a relaxation of the 97% RH observed in broken cloud layers (Albrecht et al. 1985; Betts et al. 1995) due to the coarse resolution of the radiosonde data. Figure 6b compares h determined from the radiosonde data with ceilometer measurements of cloud base height (CBH—data shown are 10th percentile of 15 min averages) measured at the CVAO during October 2007-August 2008. Given the coarse vertical resolution of the radiosonde data (of approx ±50–80 m near h) and the apparently thin clouds (Fig. 6a), CBH is expected to approximate to h, assuming that the boundary layer forcings at Sal and São Vicente are near equivalent. Unfortunately only ~90 days of radiosonde data were available over this period for comparison, but during this period CBH and h were in close agreement (Fig. 6b). The data show a strong amount of variability in inversion height over timescales of days, varying from ~300 to 1500 m, according to the synoptic conditions. However, no overall seasonal or diel pattern is evident (daily mean CBH was 713±236 m). A stratocumulus-topped marine boundary layer can exhibit strong diel modulation due to the intense longwave radiative cooling at the cloud-

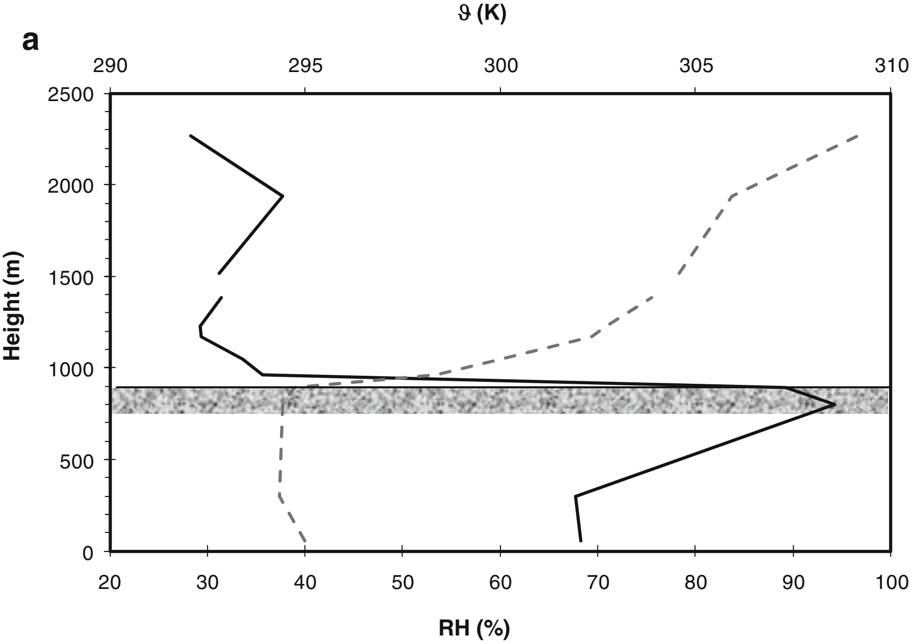

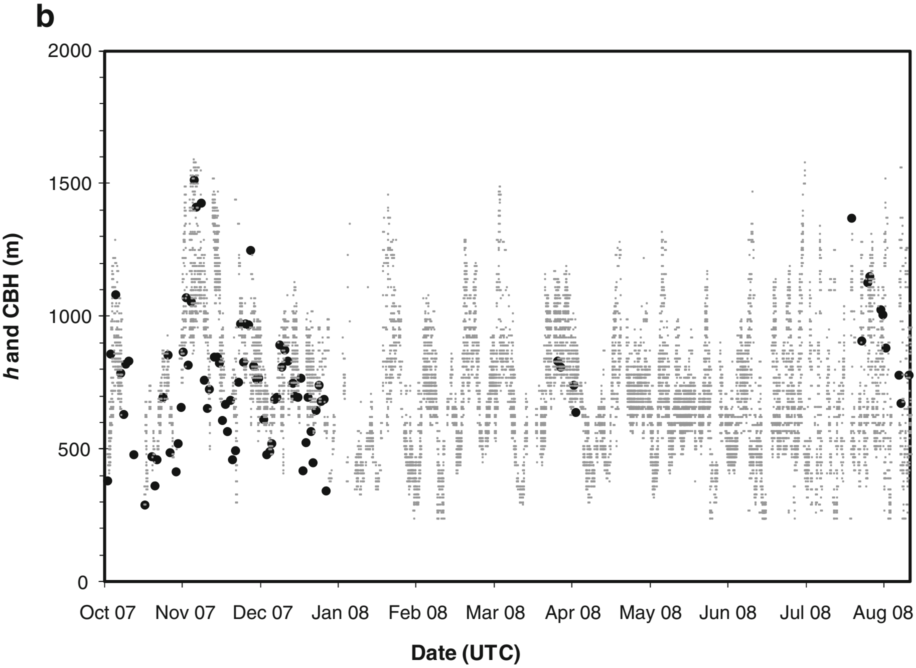

Fig. 6 (**a**) Potential temperature (θ, dotted line) and relative humidity (RH, solid line). Grey shaded area indicates cloud layer. (**b**) Comparison of ceilometer CBH (grey lines) and radiosonde *h* (black circles)

top during the night, feeding entrainment of air from the free-troposphere (Lilly 1968), and the shortwave heating of cloud top during the day, which acts to stabilize the MBL and reduce entrainment. However, in this region since no diel modulation in h is apparent, we assume that there is no systematic difference between day-time and night-time entrainment rates.

3.2.2 Radiation

Spectral radiometer measurements for the 7th March 2009 during the SOS 1 campaign as well as the variability in diurnal $J(O^1D)$ from radiometer measurements during SOS 1 are shown in Fig. 7. The suite of species' photolysis rates have a 25% absolute error bar, owing to instrument damage and calibration difficulties during the deployment, whereas the relative error (over time) is only 3%.

3.2.3 Meteorological conditions

Figure 8 shows solar radiation, wind speed and temperature and relative humidity variations from October 2006 until September 2009. Peak solar radiation occurs in May/June with maximum temperatures and relative humidity in September, whereas wind speed is variable throughout the year. Temperatures (minute averages) measured at CVAO over this period varied between 18.5°C and 31.1°C, with a mean value of 23.6°C, and relative humidity (minute averages) varied between 51 and 93%, averaging 79%

Wind speed (again from minute-averaged measurements) was between 0 and 15.8 $\mathrm{m\,s^{-1}}$ (mean and standard deviation of 6.58 ±2.30 and median of 7.33 $\mathrm{m\,s^{-1}}$) and the predominant wind direction was from the north-east as shown in the 3 year monthly wind roses in Fig. 9. Average diurnal cycles of temperature, pressure, solar radiation and relative humidity over this 3-year period are shown in Fig. 10. The solar radiation diurnal maximum occurs at 1400 UTC, whereas the temperature shows a broader diurnal maximum peaking at 1500 UTC at 24.4°C, with the mean night-time temperature only slightly lower at 23°C.

3.3 Aerosol composition and seasonality

3.3.1 Aerosol mass and major components

Saharan dust transport towards the eastern North Atlantic shows strong seasonal differences. In summer, the dust layer is found as an elevated layer up to 5–6 km, moving in a westward direction. In winter, the dust layer is transported in a south-west direction and is situated within the lowest 2 km of the troposphere and frequently transported to the Cape Verde archipelago (Chiapello and Moulin 2002; Schepanski et al. 2009). Aerosol samples collected on the island of Sal, Cape Verde between 1991 and 1994 revealed a clear seasonal cycle, with dust events occurring with significantly higher frequency and intensity during the winter months, originating from the Sahel region (south of the twentieth parallel) (Chiapello et al. 1997) (Dall'Osto et al. 2010).

The footprints computed by the NAME trajectory model also show that dust arriving at CVAO during the northern hemisphere winter (January and February) originates from the Sahel region, as well as from north-western Saharan sources and could have come from as

Fig. 7 Photolysis values for various species derived from spectral radiometers during SOS1 and focussing in on the 7th March 2009 ▶

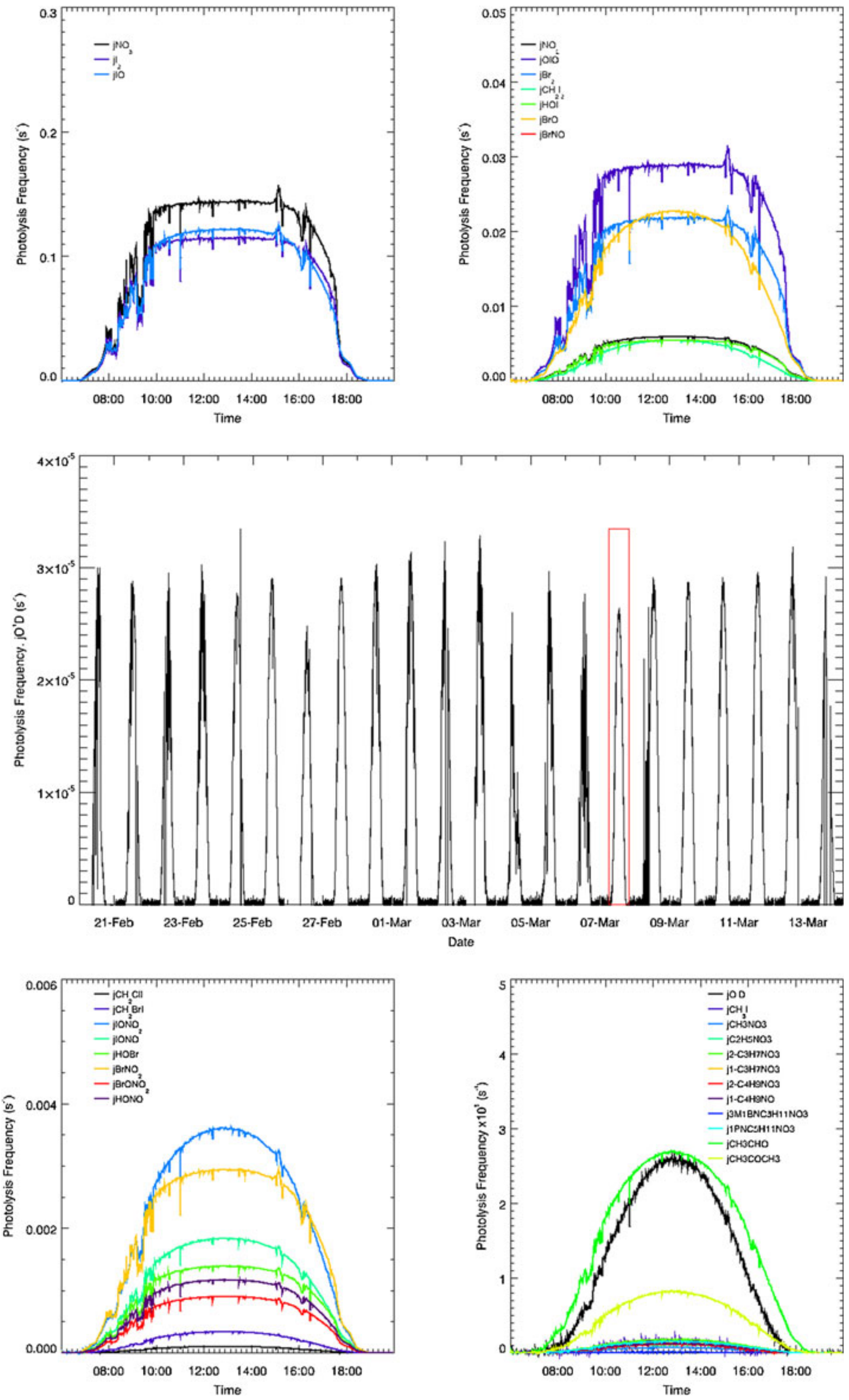
Photolysis Frequency (s⁻¹)
0.0
0.1
0.2
0.3
jNO3
jI2
jIO
08:00
10:00
12:00
14:00
16:00
18:00
Time
Photolysis Frequency (s⁻¹)
0.00
0.01
0.02
0.03
0.04
0.05
jNO2
jOIO
jBr2
jCH2I2
jHOI
jBrO
jBrNO
Time
Photolysis Frequency, jO¹D (s⁻¹)
0
1×10⁻⁵
2×10⁻⁵
3×10⁻⁵
4×10⁻⁵
21-Feb
23-Feb
25-Feb
27-Feb
01-Mar
03-Mar
05-Mar
07-Mar
09-Mar
11-Mar
13-Mar
Date
Photolysis Frequency (s⁻¹)
0.000
0.002
0.004
0.006
jCH2ClI
jCH2BrI
jIONO2
jIONO
jHOBr
jBrNO2
jBrONO2
jHONO
Time
Photolysis Frequency x10⁵ (s⁻¹)
0
1
2
3
4
5
jO¹D
jCH3I
jCH3NO3
jC2H5NO3
j2-C3H7NO3
j1-C3H7NO3
j2-C4H9NO3
j1-C4H9NO
j3M1BNC3H11NO3
j1PNC5H11NO3
jCH3CHO
jCH3COCH3
Time

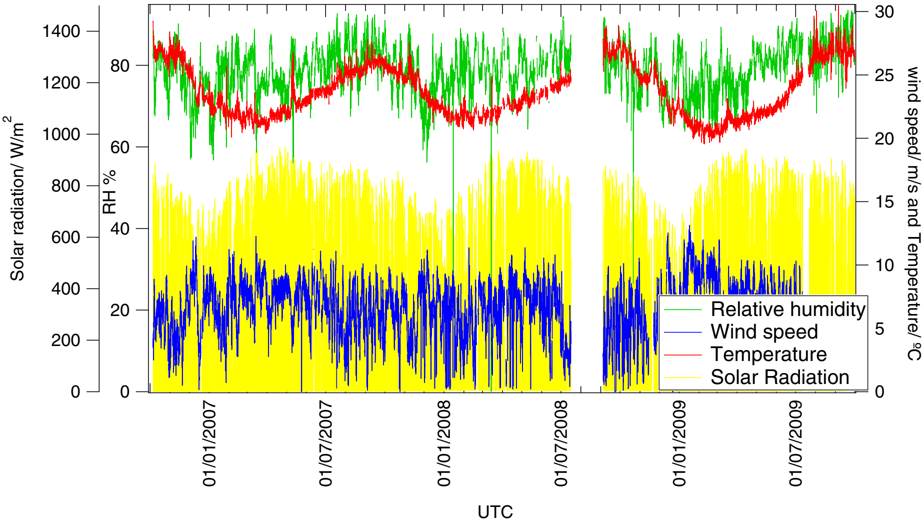

Fig. 8 Solar radiation, wind speed, temperature and relative humidity at Cape Verde

far east as the Bodélé depression in Chad (Prospero et al. 2002). The latter is the most active dust source during winter.

A clear distinction between seasons is evident in the CVAO high volume and low volume aerosol samples. In Table 2 a classification for mass concentrations collected on HV-filters was made according to season, although it should be noted that most samples were collected during the winter.

Figure 11 contrasts the aerosol size distributions in dust-influenced and marine air. In dust events, higher concentrations for diameters larger than 800 nm (coarse mode) and a nearly monomodal distribution for diameters smaller than 500 nm are observed. In contrast, a marine event shows a typical bimodal distribution for diameters smaller than 500 nm (Aitken and accumulation modes) which contribute to non sea salt (nss) sulfate. The coarse mode is smaller during the marine event, indicating that it contains predominantly sea salt particles.

The ionic composition of the aerosol at Cape Verde is dominated by sea salt but in the two smallest particulate matter (PM) classes of the size-segregated samples (<0.05 and <0.14 µm 50% cut-off sizes), non-sea salt components contributed to about 80% of the mass. Saharan dust and sea salt components were found mainly in the super-micron

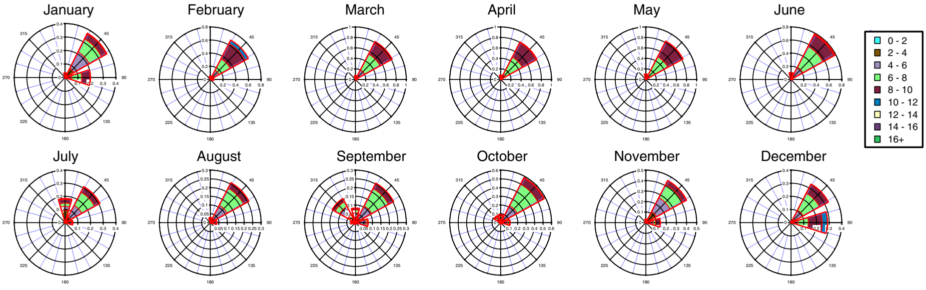

Fig. 9 Monthly wind roses for all 3 years of measurements, coloured by wind speed (m s^{-1})

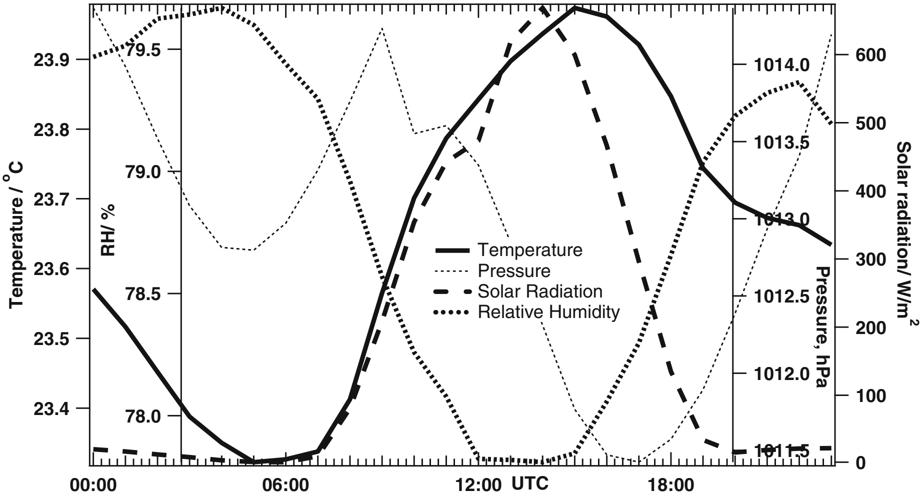

Fig. 10 Three year average diurnal cycles (UTC time (local +1 h)) for temperature, relative humidity, pressure and solar radiation

particles and less than 15% were found in sub-micron particles. Typical PM constitutions from the spring 2007 campaign are described in Müller et al. (2010).

Elemental (EC) and organic carbon (OC) were found in very low concentrations. In the smallest size fraction, OC is a major part of the PM but with increasing particle size the carbon content decreased strongly. The highest OC/EC ratios were found during dust events where continental air masses reached Cape Verde.

3.3.2 Metal composition

Strong statistical correlations are frequently found between elemental (including Fe, Al and K) concentrations in coarse mode aerosols and soils, indicating that these elements share a common crustal origin and therefore form useful indicators of Saharan dust (e.g. (Jiménez-Vélez et al. 2009)). Previous studies at Cape Verde (Chiapello et al. 1997; Formenti et al. 2003) and the Canary Islands (Kandler et al. 2007) have demonstrated the utility of elemental ratios, particularly those between Ca, K, Fe and Al, in identifying Saharan material and narrowing down source regions contributing to individual samples.

Table 2 Classification of aerosol mass concentration collected on HV-filters during January 2007- February 2010

Mass concentration classes [µg/m³]	Total	Winter Dec.-Feb.	Spring Mar.-May	Summer Jun.-Aug.	Autumn Sep.-Nov.
samples	410	177	86	77	70
> 200	17	14	1	0	2
90–200	60	40	5	1	14
60–90	43	31	3	3	6
25–60	167	53	39	41	34
< 25	123	39	38	32	14

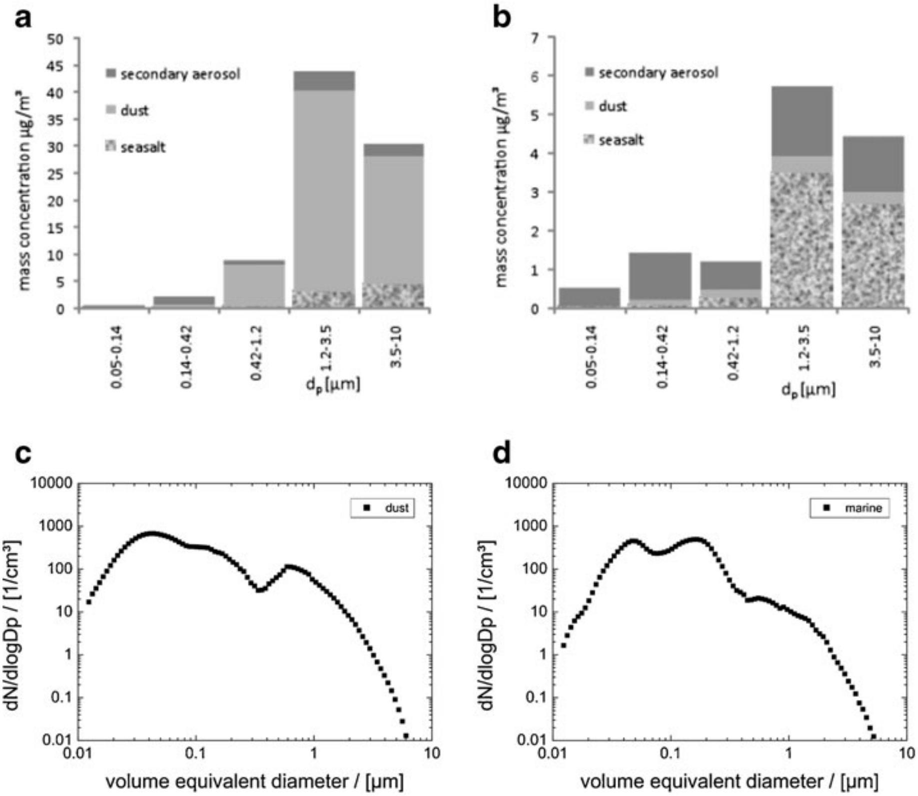

Fig. 11 Size ranges of aerosol samples and attribution of secondary aerosol, dust and sea salt from (**a**) A high dust day (8th December 2007, air masses arriving from the Sahara), (**b**) A marine influenced day (12th June 2007, air masses arriving from the northern Atlantic Ocean). The size distributions of a dust event (25th–26th November 2008), and a marine event (6th–8th July 2008) are shown in (**c**) and (**d**), respectively

The metal composition from collected size-segregated samples also showed a strong seasonal variation with more crustal metals observed during the winter intensive campaigns as compared to the spring campaigns. Figure 12 shows the iron and total PM_{10} concentration (sum of all five stages) from the 5-stage Berner cascade impactor during a winter campaign. Spikes in the figure represent Saharan dust events while dips represent days of dominant sea spray. The iron concentration showed significant differences between non-dust events and dust events (ranging between a few ng m^{-3}–4 µg m^{-3}), with iron constituting about 2% of the total aerosol mass. Most of the iron was found in larger particles i.e. of between 1.2 and 10 µm diameter. The trajectory footprints as well as the Fe/Ca and Fe/K ratios were used as criteria to distinguish the contribution of sea spray and other sources to the collected aerosols. As expected, days with higher iron concentrations are strongly correlated with Saharan dust deposition while days with low iron concentrations were associated with marine trajectories. In addition to the total iron concentration of the PM_{10} masses, the soluble Fe (II) and Fe (III) content was also investigated using an ion chromatography system with post column derivatization. These analyses are performed only during intensive campaigns.

Total Fe and Al concentrations determined from the low volume sampler between July 2007 and July 2008 are shown in Fig. 13, along with the fraction of particles originating

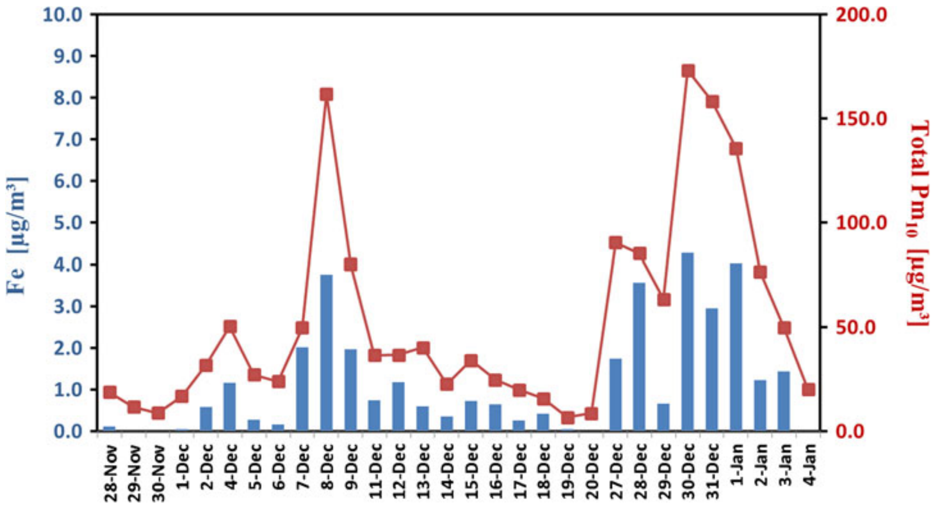

Fig. 12 Iron and total PM_{10} concentration collected by the 5-stage Berner impactor during one intensive campaign, winter 2007

from the Sahara as determined by the NAME model (section 3.1). Total atmospheric Fe concentrations varied between 0.005 and 33.4 μg m^{-3}, while total atmospheric Al concentrations ranged from 0.008 to 66.9 μg m^{-3}, with the highest concentrations occurring during the winter months (from the beginning of November to early March). Aluminium is predominantly associated with crustal materials and is often used as a tracer of mineral dust in the surface ocean (Measures and Vink 2000). Figure 13 shows several intense dust events occurring between November 2007 and April 2008. The NAME

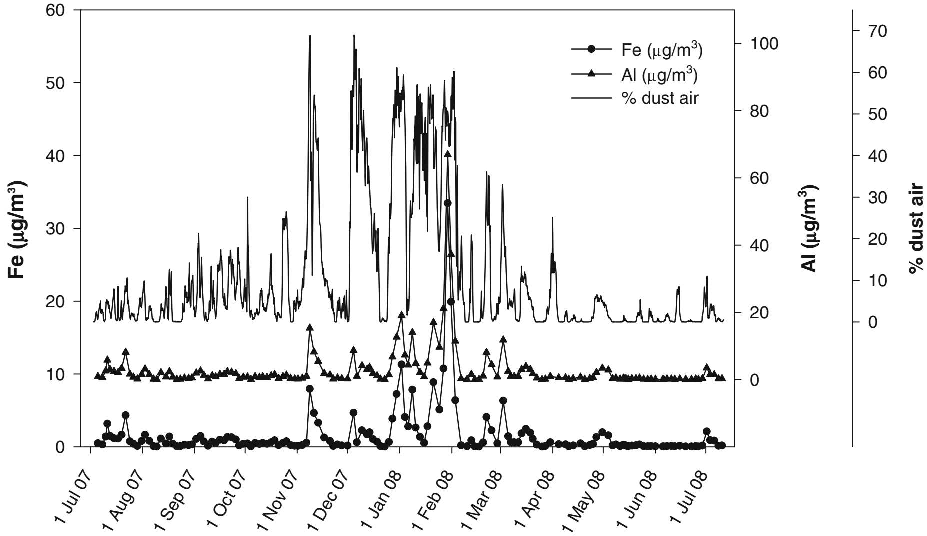

Fig. 13 Total Fe and Al concentrations in dust collected with the low volume sampler at the CVAO between 2nd July 2007 and 11th July 2008 together with the percentage of particles originating from the Sahara as calculated using the NAME model. Concentrations have been normalised to sample air volume

model captures all of these events (with a corresponding increase in the % of Saharan influence at the time) and thus we have confidence that it is correctly identifying the origin and pathways of air masses arriving at the CVAO, although clearly it cannot be used to predict the intensity of any specific dust event. During the summer months, several dust events of shorter duration and much weaker intensity can be observed. This is in line with expectations based on seasonal changes in the meteorological conditions around Cape Verde, as discussed above.

The dissolution experiments conducted using the ultrapure water leaching protocol resulted in the release of between 0.1 and 14.3% of the total Al and between 0.1 and 15.7% of the total Fe in the samples. An inverse relationship exists between the proportion of Fe and Al released and the atmospheric mineral dust concentration (using total Al concentrations as a proxy—data not shown), with much lower solubility observed at high atmospheric dust concentrations. This relationship is a ubiquitous feature among aerosol solubility datasets and there are indications that the relatively high surface area to volume ratio of smaller particles, which are dominant during periods of low dust loadings, yields a higher solubility (Baker and Jickells 2006). However, it is difficult to confirm this in an unambiguous manner since the shift to smaller particle sizes found at low atmospheric dust concentrations coincided with other changes in dust composition related to atmospheric transport (Baker and Croot 2010). Shifts in mineral composition with transport, from larger quartz grains towards more soluble clays (Journet et al. 2008) and the presence of a higher proportion of more soluble anthropogenic aerosols at low dust loadings (Sholkovitz et al. 2009) have also been proposed to explain the observed relationship between solubility and dust loading.

There was also a strong correlation between soluble Fe and Al, with a line of best fit given by $[\mathrm{Fe}]=(0.69\pm0.01)\times[\mathrm{Al}]+(0.5\pm0.7)\times10^{-3}\ \mu\mathrm{g\ m}^{-3}$; $R^2=0.95$. The different ratio of soluble Fe to Al (0.69) to the total composition (Fe/Al=0.51; $R^2=0.998$) suggests that the soluble fraction is dominated by minerals containing higher amounts of Fe relative to Al than the bulk material. For example, the strong correlation observed between soluble $PO_4^{3-}$and soluble Fe ($R^2=0.62$), indicates that the phosphate has a mainly crustal source. Some of world's largest phosphate deposits are in the source regions for Saharan aerosols (e.g. Western Sahara) (Ashley et al. 2011), and Saharan soils and aerosols have previously been shown to contain significant quantities of soluble phosphate (Herut et al. 2002; Guieu et al. 2002).

A good agreement was observed in the temporal trends for PM_{10} total Fe concentrations in samples collected using the high volume sampler and the total Fe concentrations in samples from the low volume sampler during the same time period (28th November 2007–7th January 2008) (Fig. 14). Nevertheless, total Fe concentrations were significantly higher for the period of enhanced Fe concentrations between 26th December and 5th January, although the agreement was better at the lower Fe concentrations determined earlier in the period (see Fig. 14). Some of this difference can be attributed to the difference between the PM_{10} and total suspended particle (TSP) size fractions. During periods of high mineral dust loading, there will be a greater number of larger particles, resulting in a decrease of the PM_{10} size fraction relative to TSP. However, there are experimental factors that make a simple comparison of these data difficult. The sample collection efficiency of a cascade impactor is typically lower (70–80% of TSP values) than for systems sampling TSP especially during periods of high dust loadings. Also, the longer sampling duration used with the low volume sampler and a number of periods when no samples were collected using the 5-stage Berner cascade impactor mean that it is not possible to compare samples covering the exact same time period.

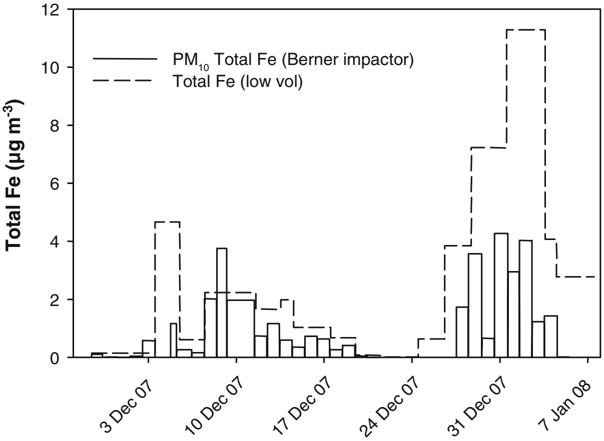

Fig. 14 Comparison of PM_{10} total Fe concentrations in samples collected using a 5-stage Berner cascade impactor and the total Fe concentrations in samples collected using a low volume sampler for the period between 28th November 2007 and 7th January 2008. Variable width bars have been used to indicate the sampling duration for the PM10 data (no sampling was undertaken between 3rd–4th December, 21st–27th December, or after 5th January). A dashed line indicates the measured Fe concentrations and sampling duration of samples collected with the low volume sampler, for which there was no break in sampling, but sampling durations were usually significantly longer than for the Berner cascade impactor PM_{10} data

3.3.3 Dicarboxylic acids and MSA in HV-samples

Several low-molecular-weight dicarboxylic acids (DCAs) were determined from both the filter samples as well as size-resolved impactor samples during the first intensive campaign. Oxalic acids were always found to be the most abundant DCAs with a mean concentration of 96 ng m^{-3} from filter samples. With increasing chain length, the mean concentrations of the DCAs decreased (malonic acid: 27 ng m^{-3}, succinic acid: 11 ng m^{-3}, glutaric acid: 3 ng m^{-3}). Among the three hydroxylated DCAs (tartronic, malic, and tartaric acid), malic acid was the most abundant (mean during first intense from filter: 4 ng m^{-3}), while the remaining two were hardly detected in the samples.

The size distributions of DCAs showed a bimodal distribution for oxalic acid and coarse mode concentration maxima for the other DCAs. As discussed in Müller et al. (2010), such distributions are commonly observed for marine aerosols and attributed to a significant fraction of the DCAs in sea salt particles.

Methanesulfonic acid (MSA) was determined together with the DCAs and a mean concentration of 37 ng m^{-3} was found from the filter samples during the first intensive campaign (Fig. 15). While a correlation with dimethyl sulphide (DMS) could not be established during that period, the MSA concentration closely followed that of nss-sulfate (Fig. 15). The size distribution showed a maximum mean concentration in accumulation mode particles ($Dp_{Aerosol}$=0.42–1.2 µm) and a similarly high concentration in sea salt particles ($Dp_{Aerosol}$=1.2–3.5 µm, (Müller et al. 2010)).

3.3.4 Amines

From theoretical calculations (Barsanti et al. 2009; Kurten et al. 2008; Loukonen et al. 2010) and field measurements (Makela et al. 2001; Smith et al. 2010) it is assumed that low molecular weight aliphatic amines can be very important in the growing process of sulfuric

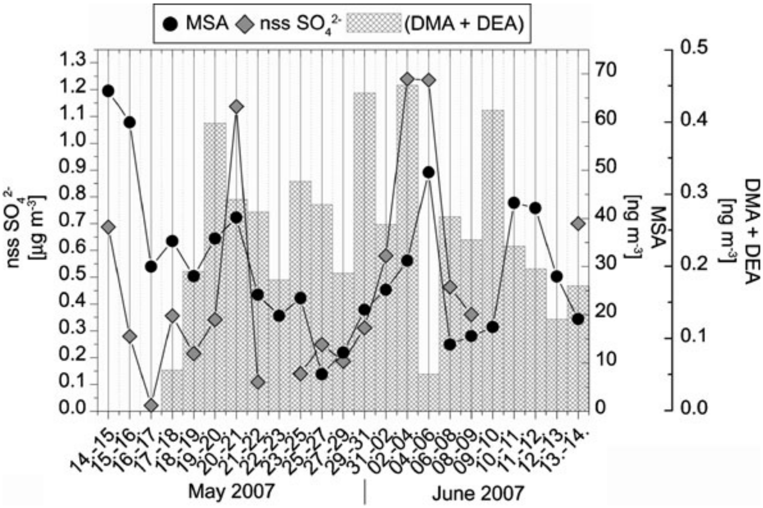

Fig. 15 MSA, nss $SO_4^{2-}$and Amines (DMA and DEA) for May and June 2007 (samples are shown as average over 2 or 3 day sampling periods)

acid clusters. Beside the influence on the physicochemical characteristics of small marine nss-SO_4^{2-}particles, the amines are also relevant for the carbon and nitrogen cycle in the marine environment (Facchini et al. 2008). Aliphatic amines, namely methylamine (MA), dimethylamine (DMA) and diethylamine (DEA), were found in the highest concentrations on stage 2 (0.14–0.42 µm) Berner impactor samples collected at the CVAO (Müller et al. 2009). The mean amine concentrations of the most abundant amines DMA and DEA varied between 270 pg m^{-3} in spring (Fig. 15) to 830 pg m^{-3} in winter 2007. However, even though the exact amine source is not known, it seems that phytoplankton is one of the major amine sources in the marine environment. A strong connection of the amines to phytoplankton activity was observed for the subtropical North Atlantic especially during an unexpected winter algal bloom in 2007/2008 (Müller et al. 2009). But, a correlation to further indicators of an enhanced phytoplankton activity such as MSA wasn't found (Fig. 15). Otherwise, there were two plausible processes identified which can be responsible for the enhanced algal growth in the winter months. These were the transport of nutrients to the surface water by local upwelling and the deposition of Saharan dust particles (3.3.2) (Müller et al. 2009).

3.4 Dust modelling

The COSMO-MUSCAT model results provide spatial context to the microphysical and chemical dust aerosol measurements at the CVAO (Heinold et al. 2011; Schepanski et al. 2009). Saharan dust transport and deposition into the tropical Atlantic Ocean were simulated for dust transport events during 2007 and up until the beginning of 2009. The model results were evaluated with in situ aerosol measurements from the CVAO, satellite dust indices and sun photometer measurements that are routinely taken at the Aerosol Robotic Network stations downwind of major dust source regions. Initial detailed comparisons of modelled dust concentrations, optical thicknesses (AOT), and particle size distributions with observations at Cape Verde show promising agreement, indicating that the model reproduces size resolved dust deposition fluxes realistically. Comparisons of

AOT time series show that the model captures individual dust transport events well. Such AOT observations have the limitation that they cannot provide information on the vertical layer structure of the dust transport.

Dust deposition is controlled by dry and wet processes. Whether dust is removed from the atmosphere as dry particles or washed out by rain can influence the chemical properties of the dust particles that are deposited into the ocean surface. In the Cape Verde region, dry deposition processes of dust dominate during most of the year, but are most pronounced in winter (Fig. 16). Dry deposition of dust particles larger than ~2 μm diameter is controlled mainly by gravitational settling and turbulent mixing to the surface. Deposition fluxes of dust particles depend on the particle size, their density and meteorological conditions along the transport trajectory and in the area where dust is deposited. After long-range transport from Saharan sources, the modelled size distribution of dust particles does not show significant variation with time, because the most important (meteorologically-driven) deposition processes are relatively independent of size. Wet deposition of particles by rain depends to some extent on particle size distribution but mainly on precipitation rates and the vertical distribution of dust layers and precipitating clouds.

Over the Atlantic, dust aerosol is transported within the Saharan Air Layer, which is a well-defined layer with low relative humidity and high dust particle concentration. Areas where wet deposition is the dominant sink of atmospheric dust are mostly influenced by convective precipitation in the intertropical convergence zone. In the summer, dust transport occurs above the marine boundary layer at 3–5 km height, and dry deposition events over

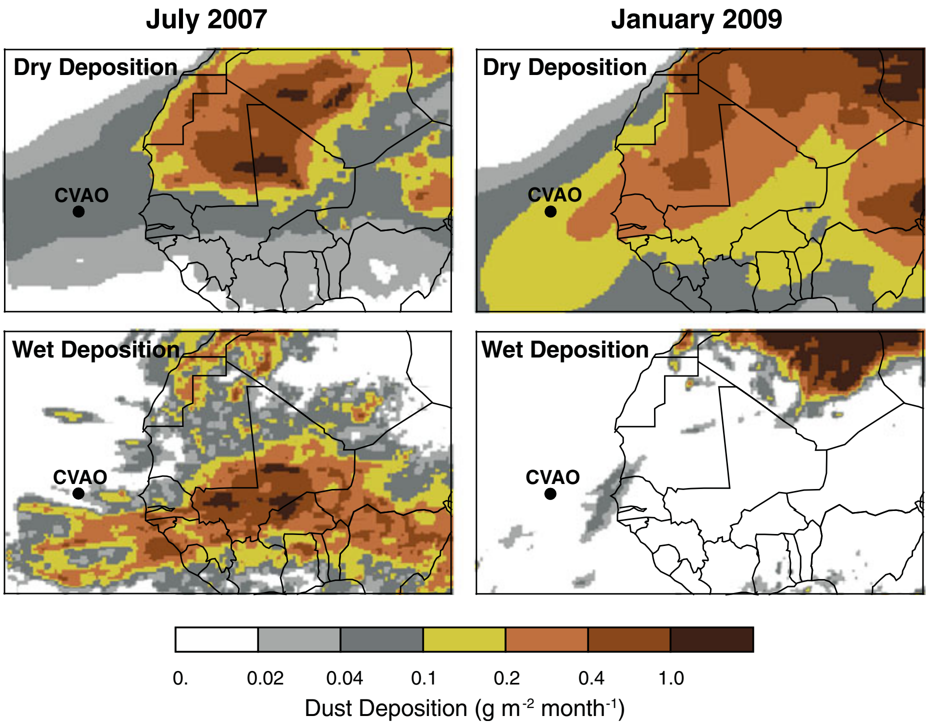

Fig. 16 Total dry (top) and wet (bottom) deposition of Saharan dust [g m^{-2}] for July 2007 (left) and January 2009 (right) simulated by COSMO-MUSCAT

the ocean are related to sinking of air masses containing dust (see also Schepanski et al. 2009). During this season deposition fluxes in the Cape Verde region are lower than in the winter months (0.04–0.1 g/m^2/month for summer compared to 0.1–0.2 g/m^2/month in winter for dry deposition, from Fig. 16) and influenced by both dry and wet processes, which occur sporadically. In contrast, Saharan dust transport in the winter months occurs in the boundary layer below 2 km height. The dust layer often extends down to the surface, which enhances dry deposition fluxes by turbulent mixing processes, while wet deposition of dust is very low in this area in winter due to very little or no precipitation, arising from the southern position of the intertropical convergence zone. In this season, when the dust layer is situated near the surface, high dust deposition rates coincide with high dust concentrations and high AOT values. Thus, in addition to providing information on the spatiotemporal distribution of dust deposition fluxes, the regional model results also point to the relevant dust deposition processes for specific dust events that are observed at the CVAO.

3.5 Greenhouse gases

The continuous observations of the greenhouse gas concentrations and O_2 exhibit synoptic events, which can be related to shifts in the trade wind system. The concentration signatures of such events are consistent with the expected signals from coastal upwelling waters. Figure 17 (right-hand side panel) shows atmospheric concentrations of CO_2, O_2, CH_4 and CO for the month of January 2009. The N_2O and SF_6 concentration records over this period do not exhibit significant excursions, and are thus not shown in Fig. 17. The data points are 2-hourly trimmed averages of the continuous measurements (i.e. discarding the 25% highest and lowest measurements in each 2-hour period). Gaps in the time series reflect malfunctioning of the instruments caused by power failures (prior to the installation of backup power generators). The Atmospheric Potential Oxygen (APO), has also been calculated and shown in Fig. 17 and represents the fraction of atmospheric O_2 variations mainly driven by oceanic processes (Manning and Keeling 2006; Stephens et al. 1998).

The left-hand side panel in Fig. 17 shows back trajectory analyses of two specific synoptic events superimposed on a map of ocean colour for January 2009, indicating monthly mean surface water chlorophyll content (from the GlobColor Project: http://www.globcolour.info). The back trajectories were computed with the HYSPLIT4 model (http://www.arl.noaa.gov/HYSPLIT.php). The colours denote trajectories before (blue), during (yellow) and after (green) the respective events. The time periods corresponding to the two synoptic events are shaded with the same colours in the right-hand side panel.

During the event of the 9th–14th January 2009 the back trajectories indicate a temporary shift of the air origin from the African coast and Canary Islands (blue and green trajectories) to the open Atlantic ocean (yellow trajectories) resulting in lower CO_2, CH_4 and CO concentrations, and higher O_2 and APO. Conversely, during the event of the 20th–27th January the air masses arriving at the site were passing over the upwelling area off Western Sahara (yellow trajectories) associated with elevated CO_2 and lower O_2 and APO concentrations. Unfortunately, CH_4 and CO measurements are unavailable for this synoptic event owing to the technical problems with the instrument. Qualitatively, the observed synoptic variations reflect the expected signatures of air-sea exchanges in the upwelling areas, which are characterised by supersaturated CO_2 and CH_4 and depleted oxygen (Kock et al. 2008; Stramma et al. 2008).

The atmospheric measurements are complemented by regular surface ocean measurements performed upstream of the CVAO at the Cape Verde Oceanic Observatory (CVOO: 17.59° N, 24.25° W) (http://cvoo.geomar.de). The combination of the atmospheric and

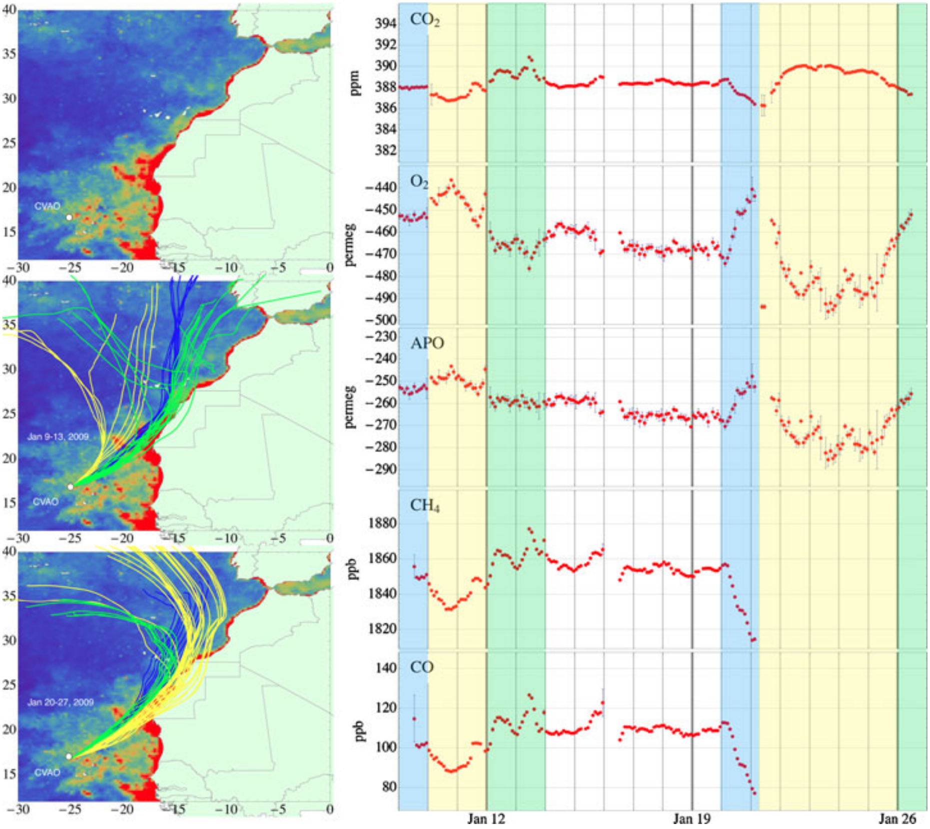

Fig. 17 Left-hand side panel: map of ocean colour with respect to chlorophyll content for January 2009, with red colours corresponding to the highest concentrations ([CHL] > 1 mg/m–^{3}). Back trajectories of air masses arriving at the CVAO (computed with the HYSPLIT4 model) are shown in different colours to denote their origin. Right-hand side panel: Atmospheric measurements of CO_2, O_2/N_2, APO (Atmospheric Potential Oxygen), CH_4 and CO shown as 2-hourly trimmed averages (including 50% of the innermost data points). Concentration units: CO_2 is shown in 'ppm', CH_4 and CO in 'ppb', and O_2/N_2 ratios and APO in 'per meg' units (a change of 1 per meg in O_2 corresponds to a change of ~4.8 ppm in CO_2). The CO_2 and O_2 are plotted so that changes can be compared on a mole per mole basis. APO is calculated from continuous measurements of CO_2 and O_2 ($APO = O_2 + 1.1\ CO_2$, where 1.1 is an average global O_2/CO_2 exchange ratio for terrestrial biosphere (Severinghaus 1995). The coloured sections correspond to the colours of the back trajectories in the left-hand side panel, and denote differences in the air mass origin

oceanic measurements at CVAO provides a unique opportunity for the long-term monitoring of a major section of the West African upwelling zone.

3.6 Reactive trace gases

3.6.1 Seasonal and sector trends of O_3, CO, VOCs and NOx

Time series of daily averaged O_3, CO, NO_x, NOy, propane, ethane, acetylene, acetone, methanol and dimethyl sulfide mixing ratios are shown in Fig. 18, plotted in UTC time (local +1 h).

O_3 displays a broad early spring maximum of 40–50 ppbv and a minimum in late summer of 10–25 ppbv, data which is consistent with other remote MBL Northern

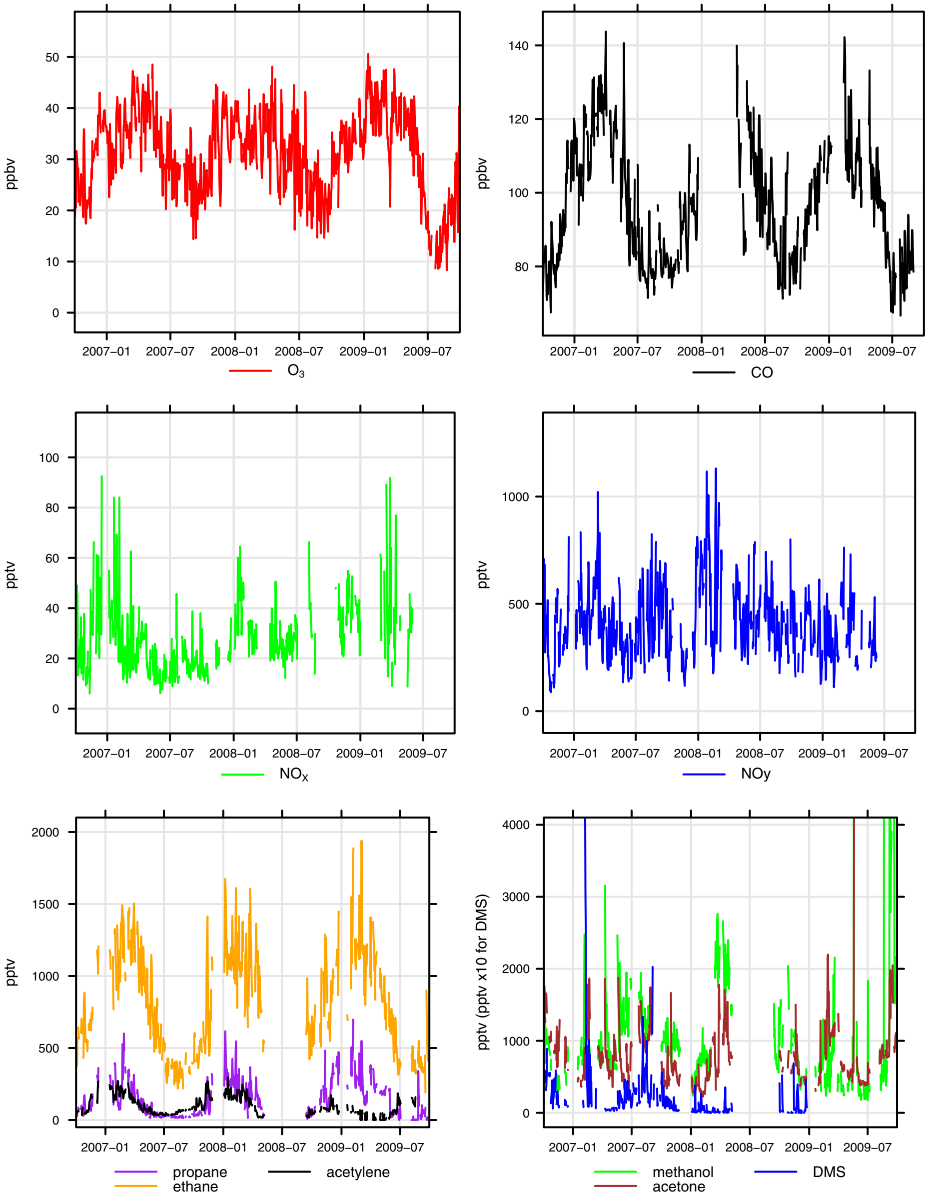

Fig. 18 Daily averaged O_3, CO, NO_x, NO_y and VOC (propane, ethane, acetylene, acetone and methanol) mixing ratios

Hemisphere sites (Monks et al. 2000; Savoie et al. 1992; Simmonds and Derwent 1991). CO and ethane levels also show spring maxima and summer minima. The CO data are very similar to measurements obtained through the NOAA flask sampling network at Azores (39º N, 27º W) (Holloway et al. 2000), a site similarly influenced by Northern Hemispheric emissions. Despite having a similar atmospheric lifetime to CO, thought to be dominated through reaction with OH, ethane shows a narrower maximum and much larger amplitude in its seasonal cycle. As discussed in Read et al. (2009) from the analysis of 2007 data, we attribute this difference in seasonal amplitude to summer time photochemical sources of CO such as oxidation of methane and OVOCs; the impact of secondary production on CO concentrations is likely to be highly relevant for the budget of this species but the current uncertainty from this source is at least a factor of three (Holloway et al. 2000; Read et al. 2009). Oxidation of ethane by Cl atoms may also play a role (Lawler et al. 2009) in the higher seasonal amplitude of ethane concentrations if Cl oxidation occurs predominantly in summer.

NO_x levels display a seasonal cycle, being generally higher during January and February and again in November and late December, as also shown by Lee et al., (Lee et al. 2009) who analysed 2007 O_3 and NO_x data. This is believed to be mainly due to increased influence of African air masses during this time, rather than photochemistry, reflecting the increased NO_x transported from the African continent, as well as NO_x that may be locally produced from transported reservoir species (e.g. PAN or HNO_3). The AFR air mass trajectories (Fig. 5) mostly originate from too far north to pick up substantial biomass burning, soil or lightning emissions of NO_x (Richter and Burrows 2002; Yienger and Levy 1995), CO and NMHC (Bechara et al. 2010; Gros et al. 2004; Hao et al. 1996) from the north African savannahs (Fig. 19), although an influence from these sources cannot be ruled out. The west African coastal cities of Dakar and Nouakchott as well as higher ship emissions from the north-east to easterly sectors, are also likely to influence NO_y and NO_x levels observed at Cape Verde. Anthropogenic emissions from coastal cities such as Dakar are advected in generally clear air and at low levels towards Cape Verde. This transport pathway contrasts markedly with that of NO_x-rich air masses associated with African soil emissions. Soil-emitted NO_x from the Sahel is stimulated by heavy rainfall events and in particular those associated with the monsoonal period (Stewart et al. 2008). In these conditions, when highly convective weather systems dominate, transport from the surface to the free troposphere via convective clouds is the dominant pathway. These conditions loft surface NO_x higher in the free troposphere such that they rarely intersect with surface measurements at Cape Verde.

Acetone, methanol and acetaldehyde levels are generally higher in early spring and in autumn. The elevated spring concentrations may be due to higher concentrations of precursor NMHCs including propane and methane at this time (see Fig. 18), which via atmospheric photooxidation represent important contributions to OVOC budgets (Lewis et al. 2005; Singh et al. 1995). After peaking in spring the OVOC concentrations tend to decrease until June, when cloud cover is at a maximum, and then start to increase at varying rates through summer and early autumn, decreasing to a minimum in December to January. The highest concentrations for acetone are observed in September. The seasonal cycle of methanol is similar to that of acetone but shows more variability with air mass trajectory; marine air masses are associated with higher concentrations in July, continental air masses contain higher methanol levels in September. For all species, high levels throughout the

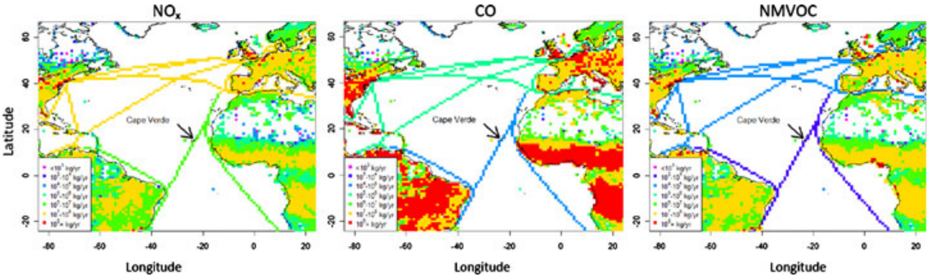

Fig. 19 NOx, CO and NMVOC emissions from the EDGAR emissions inventory (Olivier et al. 1996)

summer and autumn are likely due to increased concentrations from a combination of biogenic emissions, biomass emissions (Duncan et al. 2003), and to additional secondary chemistry due to the increased temperatures in summer (Guenther et al. 1995).

The contribution of ocean sources and sinks to the OVOC budget is at present unclear (Jacob et al. 2002; Millet et al. 2010; Millet et al. 2008). Taddei et al. (2009) observed positive (sea-to-air) zero fluxes in phytoplankton bloom areas in the remote South Atlantic but negative or zero fluxes in other ocean areas. Model calculations indicate that the ocean is a net sink for methanol, except for over the tropical Pacific (Millet et al. 2008) and generally a net source of acetaldehyde (Millet et al. 2010), but these simulations are based on only limited measurements in the remote marine environment. In order to examine potential effects of biologically-related ocean emissions on OVOC concentrations we examined their relationship with chlorophyll-A concentrations, using data classified as NCA (North American and Coastal) as representative of aged marine air which has recently passed over the upwelling. Satellite observations of oceanic chlorophyll-a coupled with back trajectory data from a Lagrangian transport model were used to calculate the average, back trajectory-weighted, chlorophyll A concentrations which the air masses arriving at Cape Verde had been exposed to, based on the method of Arnold et al. (2010). These were averaged over different time periods (1–7 days) prior to the arrival at the site, for the calendar year 2007.

The maximum in the seasonal north African upwelling (Kock et al. 2008) and in associated chlorophyll-A is during January through to April. Outside of this period, i.e. May to December, the [OVOC] do not exhibit any correlation with back trajectory-weighted chlorophyll A concentrations. However, during the peak upwelling period, acetone and acetaldehyde show weak positive correlations with chlorophyll-A ($R^2=0.37$ and $R^2=0.29$, respectively) whereas methanol does not. Methanol concentrations were on average lower during the peak upwelling period (January-April mean: 771±164 pptV, May-December mean: 1217±1149 pptV), consistent with an ocean sink for this species (Carpenter et al. 2004; Millet et al. 2008; Sinha et al. 2007). However, the seasonal nature of the upwelling means that it is very difficult to separate possible biological effects from those of other seasonal effects.

Despite all of the air masses arriving from a north-east direction (hence the position of the station on the northeast of the northern-most island in Cape Verde) and with processing occurring in the MBL for typically several days prior to arrival, the comparison of average chemical mixing ratios and their standard deviations for the seven predominant air mass types, as shown in Table 3, reveals small differences arising from the influence of relatively longer–lived sources or precursors. Some months did not experience all of the seven air mass types so do not have an average composition level.

Ozone levels were generally highest in the North American influenced air masses, reflecting relatively high levels of precursor emissions including ethane, propane, and CO from North American sources. For a given NO_2 level, higher ambient VOC concentrations will lead to ozone formation initiated by the peroxy radical (RO_2)+NO reaction, whereas lower VOC concentrations will increase the relative importance of the $OH+NO_2$ reaction, thereby favouring HNO_3 formation. Figure 20 shows an example of CO and O_3 enhancement of up to 137 ppbv and 50 ppbv, respectively, during two periods of North American influence in early 2009. Minimum levels of O_3 are in the Atlantic marine section (AM), which has no continental input for at least 10 days prior to arrival, and the African sector (AFR) in summer time. This is presumably because this sector is less photochemically aged than EUR and NAA air masses, as shown by the relatively high ratio of alkenes to alkanes and low levels of methanol (the latter associated with secondary processing of hydrocarbons) in summertime AFR air. There is also a likely influence of dust, which is a well-known sink of O_3 (see section 3.4).

Table 3 Mean, median (in brackets) and standard deviation mixing ratios of summer Atlantic (June, July, August) 2007–2009 and winter dust period (December, January, February) 2006–2009 chemical species and meteorological parameters from each air mass sector type.

SUMMER (JJA)	Atlantic and coastal AAC	Atlantic marine only AM	North American + Atlantic NAA	North American + African coast NCA	European (and coastal Africa) EUR	Africa (no European) AFR	Africa and Europe EUR/AFR
CO, ppbv	85.2 (82.4) ±11.7.2	81.5 (80.9) ±6.5	–[a]	90.8 (94.8) ±11.4	88.8 (87.4) ±11.5	81.3 (79.6) ±7.5	89.3 (82.6) ±12.7
O_3, ppbv	23.8 (24.7) ±8.4	23.9 (23.7) ±5.6	–	28.5 (29.1) ±6.7	25.2 (24.8) ±7.9	19.2 (19.6) ±5.5	23.8 (24.5) ±7.3
NO[b], pptv	3.1 (1.9) ±4.6	2.3 (1.2) ±3.6	–	2.1 (1.6) ±2.7	2.7 (1.6) ±5.4	6.0 (1.9) ±8.1	2.1 (1.3) ±3.0
Midday NO, pptv (9.00–15.00)	4.2 (3.2) ±3.6	3.1 (1.7) ±3.4	–	3.9 (3.1) ±3.8	4.5 (2.9) ±4.2	–	–
NO_2, pptv	19.1 (15.0) ±12.8	13.7 (10.6) ±8.6	–	15.9 (12.2) ±12.1	23.1 (17.6) ±15.6	30.2 (20.5) ±22.4	18.1 (14.8) ±14.4
NO_y, pptv	349.6 (329.7) ±117.5	231.7 (214.8) ±74.4	–	326.1 (319.0) ±114.5	504.2 (480.5) ±167.7	607.2 (691.7) ±236.5	621.4 (628.6) ±190.2
ethane, pptv	458.6 (414.6) ±137.5	515.9 (526.5) ±107.0	–	574.1 (522.0) ±174.4	400.6 (355.1) ±140.5	346.7 (366.5) ±52.0	255.2 (258.7) ±54.6
propane, pptv	30.2 (22.4) ±55.3	25.5 (25.1) ±13.1	–	38.6 (29.0) ±28.2	22.3 (22.1) ±12.6	28.6 (21.5) ±27.5	20.1 (21.3) ±6.6
isobutane, pptv	2.7 (2.5) ±2.7	1.2 (0.9) ±1.3	–	2.7 (2.7) ±2.1	4.3 (4.0) ±3.1	5.3 (5.2) ±1.8	4.7 (5.0) ±1.1
n-butane, pptv	4.3 (3.3) ±6.7	2.6 (2.2) ±25.8	–	4.4 (3.9) ±3.1	6.1 (3.9) ±6.2	6.4 (4.6) ±4.5	5.5 (4.4) ±3.5
acetylene, pptv	57.7 (46.0) ±31.7	52.8 (44.8) ±25.8	–	44.0 (40.4) ±11.7	54.4 (45.8) ±21.8	103.0 (73.9) ±48.7	67.0 (66.8) ±4.5
ethene, pptv	26.8 (19.0) ±38.7	16.2 (14.8) ±10.8	–	24.4 (19.3) ±21.3	26.2 (22.7) ±16.1	41.4 (25.7) ±27.2	17.6 (17.0) ±3.8
propene, pptv	17.8 (15.7) ±12.4	17.3 (17.2) ±6.5	–	21.1 (21.7) ±12.7	21.4 (18.4) ±10.6	24.3 (22.8) ±7.9	16.4 (18.0) ±4.6
methanol, pptv	1067.2 (1162.0) ±520.3	1046.8 (1159.7) ±434.2	–	1305.4 (1351.0) ±425.3	1032.5 (1052.9) ±498.7	954.6 (799.5) ±826.0	1626.5 (1595.1) ±128.5
acetone, pptv	805.2 (890.9) ±279.9	555.0 (486.9) ±221.3	–	697.9 (565.8) ±312.9	887.8 (845.5) ±327.3	791.6 (837.8) ±227.3	1571.1 (1517.1) ±452.1
Aerosol number[c], $1/cm^3$	516.2 (523.6) ±166.2	521.1 (521.0) ±158.3	–	491.1 (472.9) ±163.1	468.8 (457.9) ±134.3	567.3 (582.0) ±119.9	–
Aerosol surface area, $\mu m^2/cm^3$	82.5 (75.7) ±42.3	62.5 (60.0) ±26.0	–	92.3 (104.6) ±43.0	84.1 (82.6) ±39.1	84.3 (87.1) ±35.1	–
Aerosol volume, $\mu m^3/cm^3$	13.9 (10.4) ±9.3	7.7 (5.8) ±3.7	–	16.9 (19.3) ±10.2	15.0 (16.8) ±8.7	11.7 (11.1) ±8.0	–
Wind speed, m/s	6.1 (6.4) ±2.0	6.5 (6.6) ±1.8	–	6.8 (6.9) ±1.9	6.1 (6.4) ±2.1	3.9 (3.7) ±1.5	4.9 (4.4) ±2.3
Temperature, °C	24.6 (24.6) ±1.2	23.6 (23.5) ±0.7	–	24.2 (23.8) ±1.1	25.0 (24.8) ±1.2	25.7 (25.4) ±1.1	25.4 (25.5) ±0.9
Relative Humidity,%	82.7 (83.0) ±4.2	79.1 (79.4) ±3.5	–	81.1 (81.2) ±3.6	83.8 (83.9) ±3.5	89.5 (89.5) ±1.5	86.3 (86.5) ±3.3
Solar Radiation, W/m^2	216.0 (59.3) ±268.5	237.5 (68.7) ±283.3	–	262.2 (84.1) ±287.4	214.5 (54.7) ±265.3	96.8 (2.0) ±200.8	147.2 (18.2) ±226.4
WINTER	Atlantic and coastal AAC	Atlantic marine only AM	North American + Atlantic NAA	North American + African coast NCA	European (and coastal Africa) EUR	Africa (no European) AFR	Africa and Europe EUR/AFR
CO, ppbv	106.5 (104.8) ±8.2	109.0 (112.7) ±7.6	116.8 (116.2) ±13.1	116.0 (113.2) ±8.9	113.2 (113.4) ±9.4	104.6 (104.6) ±10.5	110.0 (109.4) ±9.8
O_3, ppbv	36.8 (37.0) ±4.8	32.8 (32.0) ±5.7	37.7 (37.2) ±5.2	39.6 (40.0) ±5.1	39.6 (39.7) ±4.4	34.8 (34.7) ±4.5	37.2 (36.9) ±3.8

Table 3 (continued)

SUMMER (JJA)	Atlantic and coastal AAC	Atlantic marine only AM	North American + Atlantic NAA	North American + African coast NCA	European (and coastal Africa) EUR	Africa (no European) AFR	Africa and Europe EUR/AFR
NO[b], pptv	2.9 (1.8) ±3.8	8.4 (4.0) ±12.5	2.7 (1.8) ±3.4	2.9 (1.9) ±3.4	3.3 (1.4) ±5.2	3.1 (1.9) ±4.3	4.0 (2.2) ±5.6
Midday NO, pptv (9.00–15.00)	4.5 (3.5) ±4.3	–[a]	5.0 (4.6) ±4.4	4.0 (2.9) ±3.2	6.0 (3.6) ±6.0	6.8 (6.0) ±5.8	9.6 (8.8) ±9.8
NO_2, pptv	24.0 (18.8) ±14.8	–	28.1 (21.4) ±22.8	29.3 (25.3) ±16.9	28.1 (27.4) ±13.8	33.0 (29.6) ±17.8	43.0 (36.0) ±22.3
NOy, pptv	389.1 (364.2) ±158.3	342.8 (333.0) ±101.5	228.9 (200.3) ±122.1	335.9 (326.4) ±118.0	453.7 (434.9) ±145.8	542.7 (493.6) ±230.4	507.5 (479.8) ±170.0
ethane, pptv	1069.5 (1044.4) ±230.6	–	1298.8 (1282.5) ±281.1	1288.2 (1339.5) ±230.9	1183.3 (1155.0) ±200.2	1155.6 (1145.0) ±190.6	1052.7 (1019.4) ±163.4
propane, pptv	227.5 (190.1) ±126.9	–	345.0 (306.2) ±161.5	328.5 (292.0) ±137.2	289.1 (270.9) ±115.7	284.0 (282.3) ±125.7	275.1 (298.1) ±89.9
isobutane, pptv	25.5 (14.1) ±21.2	–	37.3 (31.2) ±25.4	43.4 (40.9) ±19.9	35.9 (28.4) ±22.0	40.6 (36.9) ±21.7	42.0 (40.5) ±18.9
n-butane, pptv	37.0 (17.8) ±36.7	–	61.5 (47.0) ±47.0	76.6 (76.2) ±32.2	53.4 (42.3) ±37.9	63.9 (58.0) ±36.2	64.6 (65.6) ±30.9
acetylene, pptv	157.3 (152.0) ±47.5	–	174.6 (186.2) ±49.6	173.6 (186.5) ±60.0	163.1 (156.7) ±53.1	171.9 (171.5) ±57.9	156.1 (113.1) ±77.9
ethene, pptv	10.9 (14.2) ±8.1	–	34.0 (32.5) ±24.6	15.5 (16.6) ±11.4	17.3 (3.4) ±26.1	18.7 (18.9) ±10.9	16.2 (5.4) ±16.7
propene, pptv	12.7 (15.8) ±6.5	–	12.0 (10.4) ±6.5	9.5 (7.8) ±6.6	17.4 (18.1) ±5.5	9.7 (8.2) ±6.1	12.0 (11.1) ±5.4
methanol, pptv	553.8 (622.5) ±261.2	–	764.5 (741.9) ±202.5	697.4 (705.8) ±251.9	534.6 (633.0) ±280.9	728.6 (679.1) ±466.2	885.4 (787.6) ±217.1
acetone, pptv	695.7 (694.1) ±223.0	–	777.1 (765.1) ±380.6	634.1 (632.0) ±269.9	720.7 (635.4) ±392.4	694.7 (622.5) ±438.5	803.3 (563.2) ±642.5
Aerosol number[c], 1/cm^3	534.4 (554.8) ±101.5	382.5 (364.6) ±65.7	631.0 (613.7) ±212.7	559.7 (548.2) ±189.5	484.4 (510.6) ±144.4	586.9 (532.3) ±205.1	562.3 (562.5) ±112.1
Aerosol surface, μm^2/cm^3	105.4 (100.2) ±20.4	63.1 (75.8) ±24.3	111.2 (116.4) ±34.5	91.6 (88.1) ±28.6	87.0 (85.0) ±35.5	104.0 (104.5) ±36.8	99.0 (104.9) ±28.3
Aerosol volume, μm^3/cm^3	17.6 (18.5) ±3.6	9.9 (12.9) ±4.6	20.9 (21.5) ±8.1	14.6 (14.4) ±5.5	15.8 (14.6) ±8.5	16.6 (14.7) ±9.1	16.8 (16.3) ±5.7
Wind speed, m/s	7.3 (8.5) ±2.8	6.4 (7.0) ±1.6	7.2 (7.5) ±2.4	8.6 (8.9) ±2.2	8.2 (8.5) ±2.3	6.5 (6.6) ±2.2	6.4 (6.1) ±2.5
Temperature, °C	21.5 (21.5) ±0.7	22.6 (22.7) ±1.3	21.5 (21.4) ±0.7	21.6 (21.6) ±0.8	21.6 (21.6) ±0.9	22.5 (22.4) ±1.1	22.7 (23.0) ±1.2
Relative Humidity,%	77.1 (77.4) ±4.5	76.7 (75.6) ±8.8	76.3 (76.3) ±5.2	74.4 (72.7) ±5.3	74.2 (73.4) ±5.2	75.7 (76.0) ±6.0	73.7 (73.2) ±5.6
Solar Radiation, W/m^2	153.8 (13.3) ±209.5	302.1 (262.7) ±306.1	138.7 (13.1) ±195.7	144.9 (16.5) ±192.2	160.8 (22.2) ±209.7	150.7 (14.9) ±205.9	152.7 (17.7) ±201.5

[a] Values for air mass sectors with fewer than five measurements in the whole season are not shown—the North American and Atlantic air sector do not occur often in summer

[b] NO, NO_2 and NO_y have had an extra filter used to exclude all possible local contamination (excluding all local winds from south and west (100º to 360º)

[c] Aerosol measurements used for averages are only from January 2008 to October 2009

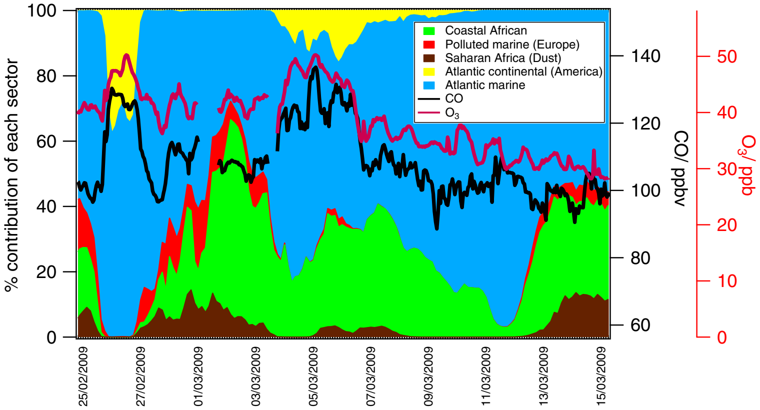

Fig. 20 Hourly averaged ozone and carbon monoxide mixing ratios and percentage contributions of the 3 hourly trajectory classifications during February-March 2009

High levels of propane and also of ethane (although less significant than those of propane) were observed in air that had passed over north Africa, probably as a result of emissions from north African petrochemical industries (Gros et al. 2004). During these events CO showed no change in concentration. Elevated levels CO from African biomass burning have been observed in the tropical east Atlantic off Africa (Gros et al. 2004), but such events have not been identified in the Cape Verde dataset. Although biomass burning will contribute to the seasonal background in CO and hydrocarbon concentrations, plumes do not directly pass over Cape Verde and so this source does not lead to strong elevations in the CO concentration.

In winter, ozone levels are similarly high in European (EUR) and North American and African coastal (NCA) air masses (whereas in summer, levels in European air masses are~ 10% lower in O_3 than in American air masses). This is likely be related to the different relative amounts of NMHC in winter and in summer: ethane levels were 38% higher in NAA compared to EUR trajectories in summer but only 11% higher in winter.

NO_2 levels were highest in the African and European air masses (AFR, EUR and EUR/ AFR). NO_y showed a similar pattern but with a greater enhancement in air masses with a Saharan origin (AFR). These trends are very similar to those found using back trajectory classifications (Lee et al. 2009). The short lifetime of NO_x means that the local mixing ratio does not give a representation of its average level during transport. The transport of nitrogen in air masses from the US to Europe is often in the form of PAN and HNO_3. These may undergo decomposition within long-range plumes re-releasing NO_x, particularly for PAN as air masses descend and reach higher temperatures. For air arriving at CVAO in summer, decomposition of PAN can be considered to be effectively complete. Previous measurements of PAN in the mid-Atlantic indicated mixing ratios ranging from more than 3 ppbv above 7 km, to below 5 pptv in the marine boundary layer (Lewis et al. 2007). This study showed that the presence of NO_x in the early and later stages of a plume trajectory typically resulted in significant elevation in O_3 in the mid Atlantic, albeit with very low in situ NO_x detected when measurements were made in the MBL.

Whilst a detailed analysis of trends is outside the scope of this paper, we note that NO_x levels appear to have slowly increased whilst O_3 and ethane levels were slightly lower in the spring of 2008 (32.9±7.0 ppbv and 993.1±289.2 pptv) than in 2007 (38.8±5.3 ppbv and 1205.5±285.3 pptv) and 2009 (37.4±5.4 ppbv and 1055.2±277.1 pptv). Meanwhile CO in spring decreased from 117.2±12.0 to 109.0±14.0 to 105.7±9.0 ppbv between 2007, 2008 and 2009. A Northern hemisphere decrease in many non-methane hydrocarbons (between 1–5% yr^{-1}) has been seen at many locations (Helmig et al. 2009) and data from CVAO appear to show a similar trend.

3.6.2 O_3/CO ratios: Influence of air mass origin and dust

Ozone to CO ratios have previously been used to estimate the amount of O_3 exported to the North Atlantic troposphere from North America (Parrish et al. 1993; Parrish et al. 1998). With a tropospheric lifetime of about 2 months, CO is a long-lived tracer of anthropogenic sources and therefore can help to differentiate between O_3 sources. The O_3/CO ratios observed at the CVAO, shown in Fig. 21, range between 0.3–0.45, very similar to the 0.3–0.4 observed at the Azores (Parrish et al. 1998). The O_3/CO ratios are higher in the African and European air masses. At a remote site such as Cape Verde, O_3 and CO enhancements are due to changes in air mass origin and mixing, rather than local emissions of CO and subsequent O_3 formation. Real et al. (2008) noted that the O_3/CO ratio in a polluted air parcel decreases as it ages and is transported further from the CO and O_3 source. The remote low latitude marine boundary layer is generally a region of low nitrogen oxide levels and high sunlight and water vapour, and thus rapid photochemistry. In such regions, O_3 and CO are simultaneously removed by photochemical processing, and aged tropical marine air (containing very low levels of nitrogen oxides) is expected to be more depleted in O_3 than CO because of its shorter lifetime. The slope of the O_3/CO ratio at Cape Verde, as observed in different air masses, correlates positively with the median NO_y level (R^2= 0.77, data not shown).

The heterogeneous reaction of O_3 (and of HNO_3 and sulphate) on mineral dust aerosol is well established by laboratory studies (Fenter et al. 1995; Hanisch and Crowley 2001, 2003). A number of global modelling studies have simulated the effect of mineral dust on O_3, and find that uptake of HNO_3 and O_3 near and downwind of the Sahara result in O_3 reductions of between 8.5% and 25% (Bauer et al. 2004; Bian and Zender 2003; Liao and

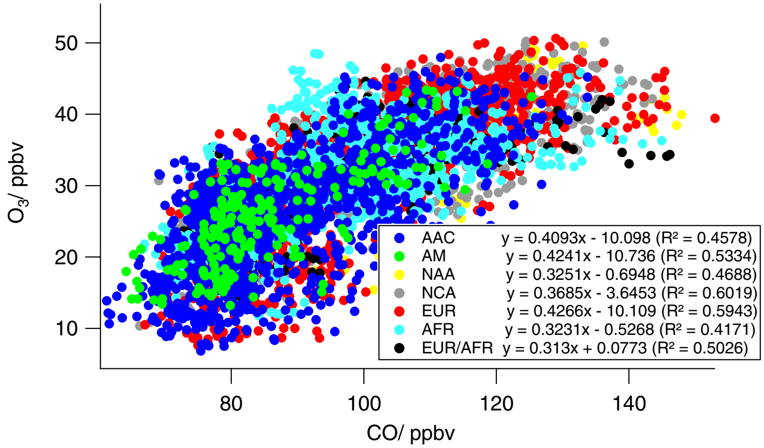

Fig. 21 O_3/CO ratios segregated by air mass classification

Seinfeld 2005; Tie et al. 2005). Mineral dust is also predicted to significantly reduce current nitrate and sulphate burdens by about 85% and by 50–70% respectively near the Sahara (Dentener et al. 1996; Liao and Seinfeld 2005). The reduction in sulphate and nitrate concentrations and associated aerosol water near the Sahara means that the presence of dust is calculated to decrease top-of-atmosphere (TOA) cooling by anthropogenic aerosols by about 0.5–1 Wm^{-2} (Liao and Seinfeld 2005).

In order to investigate the effect of dust on O_3 at Cape Verde, we plot O_3 vs CO mixing ratios in only the AFR and AFR/EUR trajectory types coloured according to the time spent over the Saharan region (Fig. 22). Overall, it is clear that there is more variation in the O_3/CO ratio in African compared to marine air. This could be due to greater variation in O_3 sources and/or in O_3 sinks, including dust uptake and also O_3 photodecomposition which will vary according to the amount of dust in the atmospheric column. The O_3/CO slope is significantly lower (0.13) for air mass trajectories with more than 40% of their time spent over the Saharan region (note that the threshold for assigning significant African influence is 9%). The results imply that in these air masses, there is a reduction of~20% O_3 at~150 ppbv CO (Fig. 22) compared to air masses with a lower influence from the Sahara. However a significant positive offset in O_3 is apparent such that at low CO concentrations, these air masses are associated with higher O_3 levels than air with a low likelihood of dust input. Respective mean NO_y values for air mass trajectories with less than 20%, more than 20%, and more than 40% of their time spent over the Saharan region were 363, 462 and 507 pptv, thus the increasing offset at higher dust influence could be due to increased photochemical production of O_3 during ageing due to higher NO_x levels. It is not clear whether the correlation between NO_y and time spent over the Sahara is due to a direct effect of the dust or an increased influence from African NO_x sources, either anthropogenic or biogenic (see section 3.6.1). If the former, this would indicate that the net result of the mineral dust is to increase the burden of NO_y, rather than a decrease through uptake of HNO_3.

3.7 Photochemical processing: HO_x radicals

3.7.1 FAGE HO_2 and PERCA $\Sigma_i(HO_2+R_iO_2)$ measurements

The warm, humid conditions and high solar irradiance experienced in the tropics lend themselves favourably to the formation of OH radicals such that peak concentrations can be as much as an order of magnitude higher than the global mean of~10^6 molecule cm^{-3} (Bloss et al.

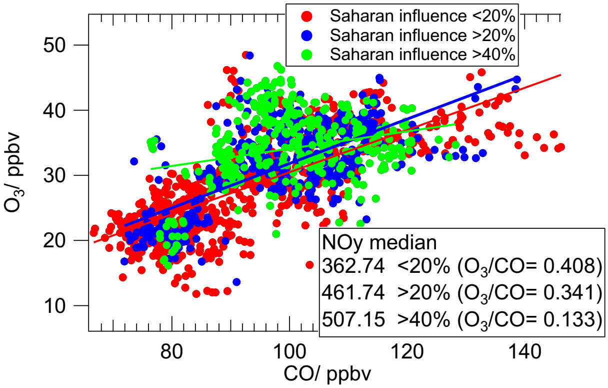

Fig. 22 CO *vs.* O_3 concentrations coloured according to the percentage of their time spent over the Saharan region

2005). In fact, it has been estimated that about 80% of methane, the third most abundant greenhouse gas (second only to CO_2 of the long-lived greenhouse gases in terms of radiative forcing (Forster et al. 2007)), is oxidised in the troposphere between 30° N and 30° S through its reaction with OH, with as much as 25% of the total occurring in marine regions (Bloss et al. 2005). Reliable, long-term measurements of OH in tropical areas are, therefore, of crucial importance for the understanding of the global oxidizing capacity of the troposphere and consequently the factors influencing climate change. However, up until recently, there have been relatively few measurements of HO_x (i.e. OH and HO_2) in tropical regions compared to in polar or mid-latitude areas, and none over a time-span sufficient to investigate their seasonality. Peroxy radicals ($HO_2+\Sigma_i R_i O_2$) are key intermediates and chain carriers in the photochemical cycling of ozone in the troposphere e.g. (Monks 2005). Peroxy radicals are formed via the oxidation (mainly by OH) of anthropogenic and biogenic species in the atmosphere such as CO, CH_4 and other organic compounds. Ozone is produced via the peroxy radical catalysed oxidation of NO to NO_2 and subsequent photolysis of NO_2, whilst ozone can also be destroyed through reaction with HO_2 (Monks 2005). Owing to the short lifetime of peroxy radicals (HO_2 has a lifetime on the order of a minute in clean air, much less than a minute in polluted air (Monks 2005)), they give a good indication in combination with NO of in situ photochemical ozone production and loss. In addition, the self- and cross-reactions of peroxy radicals to form peroxides (e.g. H_2O_2) are a major sink for HO_2 and OH (Reeves and Penkett 2003).

HO_x measurements made by the FAGE instrument during the May-June 2007 RHaMBLe period are reported in Whalley et al. (2010). Maximum concentrations of OH and HO_2 were 9×10^6 molecule cm^{-3} and 6×10^8 molecule cm^{-3}, respectively. A decrease in daily peak [HO_2] was observed, coinciding with a decrease in CO concentrations and a shift in the sampled air mass originating from the western north Atlantic (AM) and continental America (NAA) to air from Southern Europe and the Mediterranean (EUR). A modelling study based on the Master Chemical Mechanism (MCM) showed that the observations could be reproduced to within the 20% (1σ) uncertainties if aerosol uptake and the chemistry of IO and BrO were considered. The model was most sensitive to changes in the aerosol parameters and the concentrations of BrO, IO and formaldehyde.

During the SOS campaigns in 2009, the February-March period had an average temperature of~21°C with some days of significant cloud cover and periods of short, light rain showers. The June measurement period was driest, with an average temperature of~23°C whereas the September period had diverse weather conditions with days of torrential rainfall (for example, 14–15th) interspersed with some days of strong sunlight and higher average temperatures (~30°C). The highest peak values of $J(O^1D)$ were observed during this period.

The median diurnal profiles of hourly-averaged FAGE [OH], [HO_2], [HO_2]/[OH] and $J(O^1D)$ (as recorded by the University of Leeds (UOL) radiometer) for each of the three SOS campaigns and the RHaMBLe campaign are plotted in Fig. 23; the error bars are one standard deviation of the hourly-averaged [OH] and [HO_2], and for clarity, are only shown for SOS 2 and RHaMBLe, which were measured at similar times of the year. The daytime concentrations of both OH and HO_2 tended to increase through 2009 (*i.e.* SOS

Fig. 23 Median hourly-averaged OH, HO_2 (as measured by the FAGE instrument) and $J(O^1D)$ levels recorded during SOS1 (black line), SOS2 (red line), SOS3 (green line) and RHaMBLe (blue lines); (**a**) concentrations and mixing ratios of OH (for clarity, only the error bars showing the 1σ of the hourly-averaged data for SOS2 and RHaMBLe are shown); (**b**) concentrations and mixing ratios of HO_2 (only the error bars showing the 1σ of the hourly-averaged data for SOS2 and RHaMBLe are displayed); (**c**) the ratios of [HO_2] to [OH] (only values for between 8AM and 5PM have been shown for clarity); (**d**) PERCA HO_2 + ΣRO_2; (**e**) values of $J(O^1D)$ measured using the University of Leeds' radiometer (the blue solid is for OH-measuring period, blue dotted is for HO_2 measuring period during RHaMBLe, respectively) ▶

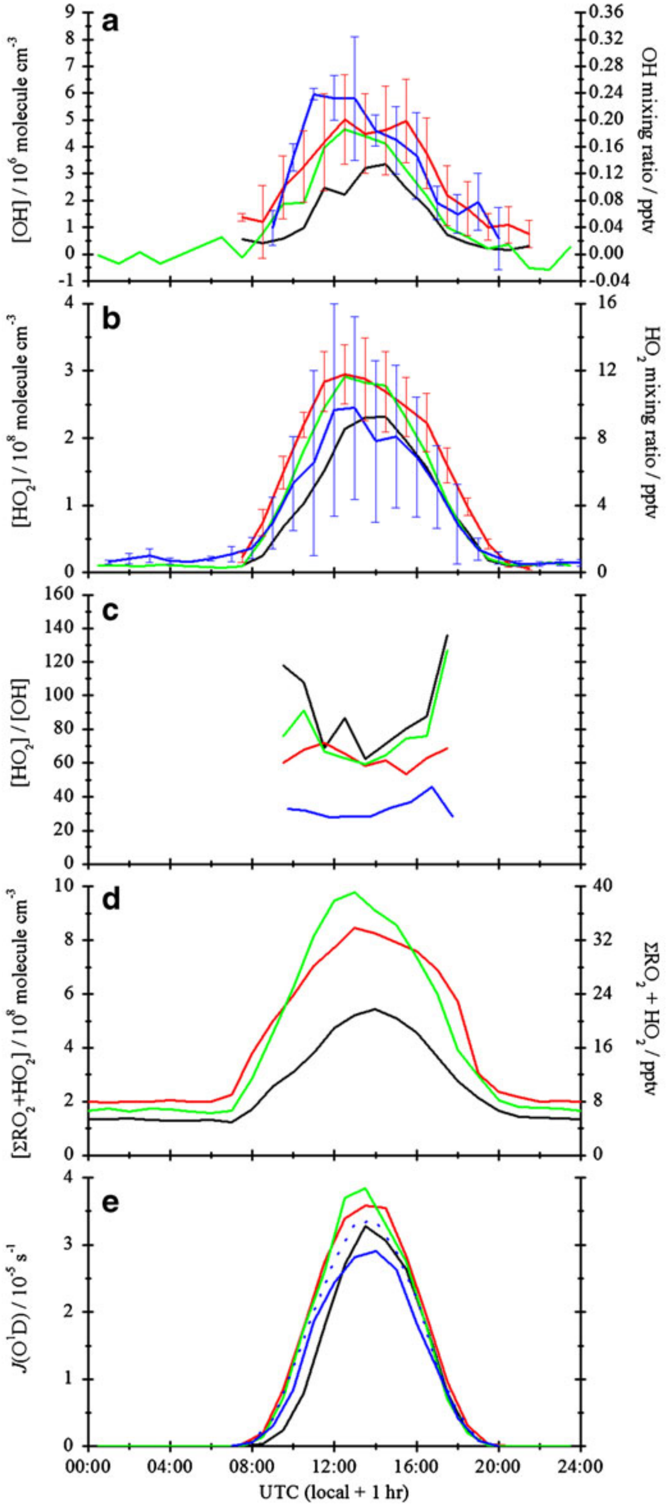
a
[OH] / 10^6 molecule cm^-3
-1
0
1
2
3
4
5
6
7
8
9
OH mixing ratio / pptv
-0.04
0.00
0.04
0.08
0.12
0.16
0.20
0.24
0.28
0.32
0.36
b
[HO2] / 10^8 molecule cm^-3
0
1
2
3
4
HO2 mixing ratio / pptv
0
4
8
12
16
c
[HO2] / [OH]
0
20
40
60
80
100
120
140
160
d
[ΣRO2+HO2] / 10^8 molecule cm^-3
0
2
4
6
8
10
ΣRO2 + HO2 / pptv
0
8
16
24
32
40
e
J(O1D) / 10^-5 s^-1
0
1
2
3
4
00:00
04:00
08:00
12:00
16:00
20:00
24:00
UTC (local + 1 hr)

3>SOS 2>SOS 1), consistent with the increase in parameters key to their formation (e.g. $J(O^1D)$ and H_2O). HO_2 concentrations were on average higher, and OH slightly lower, during SOS 2 compared to the 2007 RHaMBLe data, and consequently the daytime $[HO_2]$:[OH] ratio observed during SOS 2 was about twice that of RHaMBLe. However, it should be noted the concentrations of each species during June 2007 and 2009 were within the respective 1σ day-to-day variability represented by the error bars. This agreement could suggest that there may have been similar influences (e.g. levels of halogen oxides, aerosols) on HO_x-budgets at the site during both timeframes. The full statistical and modelling analyses of the 2009 dataset carried out by Vaughan et al. (2011) investigates in more detail the factors causing the seasonal and day-to-day variability of HO_x and their consequent impact on atmospheric processes.

Figure 23d shows the mean hourly average diurnal cycle $HO_2+\Sigma_iR_iO_2$ measurements made by the PERCA instrument during the three SOS intensive periods. Similarly to Fig. 23b, the diurnal cycles show a classical bell shape with a slight asymmetry ascribed in previous low NO_x marine boundary layer studies to the persistence of RO_2 radicals (Monks et al. 1996) into the night owing to the relative rates of radical cross and self-reactions. It is clear that the maxima in radical concentration scales with season. The maxima in $J(O^1D)$ (measured by UOL), the primary driver for radical production in the remote marine boundary layer were 3.28×10^{-5} s^{-1}, 3.58×10^{-5} s^{-1} and 3.84×10^{-5} s^{-1} during SOS 1, SOS 2, and SOS 3.

Both the FAGE and PERCA instruments showed a similar trend in increasing concentrations of peroxy radicals from SOS 1 through to SOS 3 (although it must be noted that the two instruments did not run simultaneously during SOS 2 because of technical difficulties with the FAGE set-up). The maximum contributions of HO_2 (as measured by FAGE) to the hourly-averaged daytime budget of total peroxy radicals (as measured by PERCA) were 40%, 45% and 34% for SOS 1, 2 and 3, respectively. Measurements in the Borneo rainforest in 2009 in the OP3 campaign (Hewitt et al. 2010) gave HO_2/HO_2+RO_2 an average ratio of 15% for day light hours (Arunasalam personal communication), similar to the approximate 10% daily maximum ratios during the OOMPH Southern Ocean cruise (Hosaynali Beygi et al. 2011) but daylight ratios at Mace Head, Ireland were between 10 and 40% on low NO_x days and up to 70% on high NO_x days in summer 2002 (Fleming et al. 2006).

The PERCA data show that RO_2 persisted through the night-time, up to levels of~10 pptv. The FAGE system was only able to be run through one night, during SOS 3. Low levels of HO_2 (< 1 pptv) were observed that evening implying that HO_2 contributed less than 10% of the night time peroxy radical budget, at least for that night. This is as expected in the clean marine boundary layer, where the lifetime of RO_2 at night (with NO absent) is much longer than that of HO_2, as discussed above (Monks et al. 1996). Whalley et al. (2010) also observed low night-time levels of HO_2 (~ 0.6 pptv) during RHaMBLe. However, these levels were significantly higher than night-time levels predicted by the MCM, and those authors showed that air masses with a high content (~ 100 ppt) of peroxyacetyl nitrate (PAN) could reproduce their night-time observations. This conclusion remains untested due to a lack of seasonal PAN measurements at the CVAO, although PAN concentrations as high as 120 pptv were observed by Jacobi et al. (1999) during a cruise off the west coast of Africa, north of 10 ° N.

In the clean atmosphere around Cape Verde, formaldehyde (HCHO) is also important for the HO_x budget. LP-DOAS observations show that typical HCHO mixing ratios ranged between 350–550 pptv, with several events of high HCHO up to 1885±149 pptv (Mahajan et al. 2010b). The data indicate a lack of strong annual or diurnal trend within the uncertainty of the measurement. The observed levels of HCHO are below the detection limit of satellite observations at this altitude, even during the high HCHO episodes. Modelling results suggest that the typical diurnal profile and monthly mean values can be replicated well using the methane and NMHC observations and that on average 20% of HO_2 production and 10% of OH destruction can be attributed to the mean HCHO levels (Mahajan et al. 2010b; Whalley et al. 2010).

3.8 Halogen chemistry

IO and BrO were observed ubiquitously during the day by the UOL LP-DOAS with daytime (0900–1700 GMT) mixing ratios plateauing at around 1.5 pptv IO and 2.5 pptv BrO during the first period (November 2006–June 2007) (Mahajan et al. 2010a; Read et al. 2008). The seasonal changes for both species were within the variability of the dataset. Detailed 1-D modelling of the sources of halogens and their impact on the boundary layer chemistry by Mahajan et al. (2010a) indicates that the IO and BrO account for up to 45% of the observed O_3 destruction at the surface around Cape Verde. In addition, we suggest that an extra iodine source from the surface is necessary and is most probably photolysis dependent (Mahajan et al. 2010a), because the observed fluxes of iodocarbons account for only 10–25% of the observed IO (Jones et al. 2010). The modelling work also indicated a strong vertical gradient in the IO mixing ratios, with the value at 500 m falling by 90% compared to the observed surface IO.

The retrieved University of Heidelberg UOH MAX-DOAS BrO values were under the detection limit of 4.4 pptv. The IO concentrations were comparable with the UOL LP DOAS results (Read et al. 2008). Vertical profiles of IO retrieved from the UOH MAX-DOAS measurements indicate that IO is present in a shallow layer with a vertical extent ranging between 100 and 500 m, in agreement with the modelling discussed above. The daily averaged IO concentration at the surface as determined from the MAX-DOAS data was of the order of 1.5 pptv. This value is however the subject of substantial, currently not completely understood, uncertainties owing to the limited information on the viewing conditions. In contrast to both the UOH MAX-DOAS measurements and the UOL LP-DOAS measurements, data from UOH LP-DOAS measurements performed from June-October 2010 show no IO values above the detection limit of typically 0.6 pptv. Also, CE-DOAS observations in June 2010 show no IO concentrations above the detection limit of typically 2 pptv. A reason for the lower IO levels than observed by UOL may be due to changed atmospheric conditions or measurement errors. Further studies on the different observed IO levels are necessary. LP-DOAS BrO concentrations are in good agreement with UOL observations, with daytime averages of 3.0 pptv (Fig. 24), but with strong variations from day to day, peak concentrations in the morning and evening, and a clear minimum at noon. However, the morning and evening peak occur at different times from day to day due to different metrological conditions and are not apparent in the mean daily concentrations over the 9 day measurement period. Peak mixing ratios of up to 6 pptv were observed on several days between June and October 2010. The vertical UOH LP-DOAS distributions (using reflectors at different heights) show a well mixed BrO layer within the lower 100 m and a decrease to almost half the surface concentrations between 92 and 560 m (Fig. 24).

4 Summary and future perspectives

Long term measurements are central to the understanding of atmospheric composition and its impact on climate. Whilst the data sets obtained at CVAO are not yet sufficient to detect trends, we have presented information on inter- and intra-annual and diurnal cycles of surface trace gases and aerosol, with air mass trajectories and influences characterised by the NAME dispersion model. These show a strong influence from Saharan dust in winter, a year-round

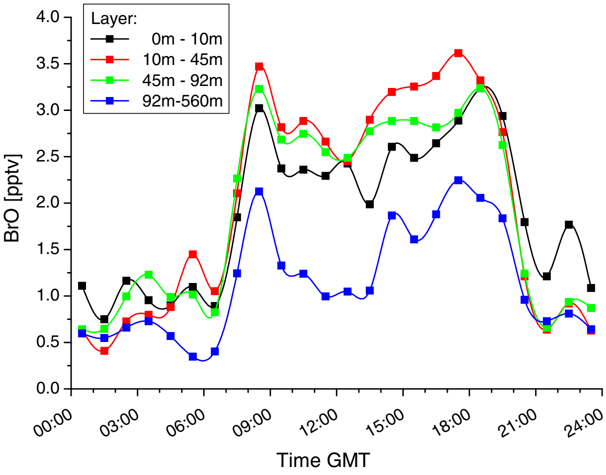

Fig. 24 Averaged daily cycle of BrO concentration with the UOH LP-DOAS instrument for different layer heights (vertical profile) derived from measurements to retro reflectors at different heights on the mountain of Monte Verde between the 12th and 20th June 2010. A maximum peak concentration in the morning after sunrise and evening at sunset with a local minimum at noon was observed.

presence of ocean-derived organic and inorganic components in gaseous and particulate form which have impacts on aerosol formation and oxidation chemistry, and long range transport of O_3 precursors from North America and Europe especially in spring/summer.

Saharan dust and sea salt dominate the super-micron aerosol particles at Cape Verde. Iron constituted a few % of the total aerosol mass of the super-micron dust, with aluminium, a tracer of mineral dust, at slightly higher concentrations. Both metals show highest concentrations in the winter months. The NAME model captured all of the dust events, showing that it correctly identifies the origin and pathways of air masses arriving at the CVAO, although it cannot be used to predict the intensity of a certain event. The COSMO-MUSCAT dust model was evaluated with in situ aerosol measurements from the CVAO as well as remote sensing data and showed promising agreement, indicating that the model reproduces size resolved dust deposition fluxes realistically. The model shows that in the Cape Verde region, dry deposition dominates the deposition of dust during most of the year. Saharan dust transport in the winter months occurs in the boundary layer below 2 km height and often extends down to the surface, which enhances the dry deposition flux. Whether dust is removed from the atmosphere as dry particles or washed out by rain can influence the chemical properties of the dust particles that are deposited into the ocean surface. Dissolution experiments on collected dust samples resulted in the release of between 0.1 and 14.3% of the total Al and between 0.1 and 15.7% of the total Fe, with a strong correlation between soluble Fe and Al and much lower solubility measured at high atmospheric dust concentrations. The higher ratio of soluble Fe to Al compared to the total composition suggests that the soluble fraction is dominated by minerals containing higher amounts of Fe relative to Al than in the bulk material, e.g. phosphate.

The ionic composition of the aerosol at Cape Verde is dominated by sea salt but in particles below<0.14 μm diameter, non-sea salt components contributed about 80% of the mass. These components include low-molecular-weight dicarboxylic acids (DCAs) and hydroxylated DCAs, methanesulfonic acid (MSA) and aliphatic amines. A bimodal size distribution for the DCA oxalic acid and coarse mode concentration maxima for the other DCAs were observed, as is typical for marine aerosols. The MSA concentration closely followed that of non-sea-salt-sulfate and the size distribution showed a maximum mean concentration in accumulation mode and in sea salt particles. Aliphatic amines, assumed to be important in the growing process of sulfuric acid clusters, were correlated with phytoplankton activity in the subtropical North Atlantic, especially during an unexpected winter algal bloom.

Levels of ozone, CO and anthropogenic VOCs, including ethane and propane, show spring maxima and summer minima, in line with previous northern hemisphere observations, and were generally higher in the North American influenced air masses. In contrast, the OVOCs showed a broad summer maximum, highest in the AFR/EUR sector, and with some evidence for a coastal/upwelling source of acetone and acetaldehyde. O_3/CO ratios were between 0.3–0.45, highest in European air masses that contain relatively less well aged air with less opportunity for O_3 photochemical destruction. In air heavily influenced by Saharan dust, the O_3/CO ratio was as low as 0.13, although with a significant positive offset in O_3. The opposing effects of O_3 uptake to dust and increased photochemical production of O_3 during ageing due to higher NO_x levels in African air make interpretation of these data difficult. NO_x and NO_y were most abundant in the African and European air masses and showed generally higher concentrations in winter when air mass origins are predominantly from Africa. This likely reflects biomass burning and soil emissions from the Sahel and local production of NO_x from transported reservoir species (e.g. HNO_3 and PAN), with possible contributions from west African coastal cities and higher ship emissions from the northeast to easterly sectors. A more complete analysis of influences and impacts of nitrogen oxides at Cape Verde will be the subject of a future publication.

High photochemical activity is evident at this tropical location, with maximum concentrations of OH and HO_2 of 9×10^6 molecule cm^{-3} and 6×10^8 molecule cm^{-3}, respectively. The maximum contributions of HO_2 (as measured by FAGE) to the hourly-averaged daytime budget of total peroxy radicals (as measured by PERCA) were~35–45%, rather higher than previously measured ratios in low NO_x conditions (Fleming et al. 2006; Hosaynali Beygi et al. 2011) presumably due to low VOC/CO ratios in the very clean air at Cape Verde. Model simulations of HO_x could reproduce observations to within uncertainties if HO_x aerosol uptake and the chemistry of IO and BrO were considered, and were most sensitive to changes in the aerosol parameters and to the concentrations of BrO, IO and HCHO. Typical HCHO mixing ratios ranged between 350–550 pptv and, as expected from their dominant source from methane and NMHC, did not show strong inter-annual variation. Little diurnal variation in HCHO mixing ratios is observed because the sources (mainly hydrocarbon oxidation) and sinks (mainly photolysis and OH oxidation) are predominant during daytime and balance each other in this clean background environment.

IO and BrO were ubiquitously observed by the UOL LP-DOAS during the day at Cape Verde with maximum daytime mixing ratios of~1.5 pptv IO and~2.5 pptv BrO during the period November 2006–June 2007. UOH MAX-DOAS observations indicated similar levels of IO (~ 1.5 pptv, albeit with substantial uncertainties due to retrieval assumptions) in a thin layer of 100 m up to 500 m. Model simulations indicate a strong vertical gradient in the IO mixing ratios, consistent with these observations. However, the UOH IO LP-DOAS and CE-DOAS observations show substantially different results for IO, with no observations above the detection limits of these instruments of 0.5 and 2.0 pptv, respectively. The differences between the IO concentrations during the period 2006–2007 and 2010 indicates either decreasing IO concentrations after 2007 or possible measurement interferences (e.g. stray light) for IO with the DOAS method. UOH LP-DOAS data from June-October 2010 showed BrO average daytime mixing ratios of ~3.0 pptv, similar to the UOL LP-DOAS measurements (Read et al. 2008). Maximum values in the morning and evening, a local minimum at noon, and a strong variability from day to day with peak mixing ratios up to 6 pptv were observed. The BrO observations do not show a strong vertical gradient, indicating that it is well mixed in the boundary layer. Detailed 1-D modelling indicates that the IO and BrO account for up to 45% of the observed O_3 destruction at the surface around Cape Verde.

The retrieval of aerosol extinction profiles from MAX-DOAS O_4 measurements is a relatively new technique, and has so far only been applied to CVAO data for some selected days. A comprehensive analysis of the MAX-DOAS measurements planned for the near future will provide aerosol extinction profile data which is not only useful for the improvement of the accuracy of the MAX-DOAS trace gas retrieval, but also valuable for the investigation of the aerosol vertical distribution during Saharan dust events and their impact on the atmospheric radiation budget.

Finally, radiosonde and ceilometer data shows a strong amount of variability in inversion height over timescales of days, varying from~300 to 1500 m. Thus, simple box models which assume invariant boundary layer heights are unlikely to simulate chemical variability accurately. No overall seasonal or diurnal pattern was evident in boundary layer heights, indicating no systematic difference between day-time and night-time entrainment rates.

Future studies at the Cape Verde Atmospheric Observatory Humberto Duarte Fonseca (CVAO) aim to build on the data presented herein, for example by elucidating the nature and magnitude of oceanic iodine emissions, quantifying the nitrogen oxides budget, evaluating the influence of dust on the ocean heat budget, understanding oceanic nitrogen fixation and quantifying air-sea exchange fluxes of carbon dioxide, oxygen, methane and nitrous oxide in the west African upwelling area.

Acknowledgements We would like to thank all the scientists involved in measurements at the Cape Verde Atmospheric Observatory (CVAO) and during the RHaMBLe campaign in 2007 and the SOS campaigns in 2009. We would like to thank NOAA for the ESRL radiosonde data from the island of Sal. We would like to thank R. Leppert, R. Schwalbe and T. Seifert (MPI-BGC) for technical support for the greenhouse gas measurement equipment. We would like to acknowledge Pete Edwards and Andy Goddard from the University of Leeds for their technical support throughout the campaign and the UK Meteorological Office for the use of the Unified Meteorological data and the NAME model. We acknowledge funding from the NERC SOLAS program, the National Centre for Atmospheric Science (NCAS) through FGAM (Facility for Ground based Atmospheric Measurements), the EU specific Support Action TENATSO, and the SOPRAN project of the German Federal Ministry of Education and Research.

References

Albrecht, B.A., Penc, R.S., Schubert, W.H.: An observational study of cloud-topped mixed layers. J Atmos Sci **42**(8), 800–822 (1985)

Arnold, S.R., Spracklen, D.V., Gebhardt, S., Custer, T., Williams, J., Peeken, I., Alvain, S.: Relationships between atmospheric organic compounds and air-mass exposure to marine biology. Environ. Chem. **7**(3), 232–241 (2010)

Ashley, K., Cordell, D., Mavinic, D.: A brief history of phosphorus: From the philosopher's stone to nutrient recovery and reuse. Chemosphere **84**(6), 737–746 (2011)

Baker, A.R., Jickells, T.D.: Mineral particle size as a control on aerosol iron solubility. Geophys. Res. Lett. **33**(17) (2006)

Baker, A.R., Croot, P.L.: Atmospheric and marine controls on aerosol iron solubility in seawater. Mar. Chem. **120**(1–4), 4–13 (2010)

Baron, P.A., Willeke, K.: Aerosol Measurement. In., vol. 2nd Edition. J. Wiley and Sons, (2001)

Barsanti, K.C., McMurry, P.H., Smith, J.N.: The potential contribution of organic salts to new particle growth. Atmos Chem Phys **9**(9), 2949–2957 (2009)

Bauer, S.E., Balkanski, Y., Schulz, M., Hauglustaine, D.A., Dentener, F.: Global modeling of heterogeneous chemistry on mineral aerosol surfaces: Influence on tropospheric ozone chemistry and comparison to observations. J. Geophys. Res. **109,** D2 (2004).

Bechara, J., Borbon, A., Jambert, C., Colomb, A., Perros, P.E.: Evidence of the impact of deep convection on reactive Volatile Organic Compounds in the upper tropical troposphere during the AMMA experiment in West Africa. Atmos Chem Phys **10**(21), 10321–10334 (2010)

Behrenfeld, M.J., O'Malley, R.T., Siegel, D.A., McClain, C.R., Sarmiento, J.L., Feldman, G.C., Milligan, A. J., Falkowski, P.G., Letelier, R.M., Boss, E.S.: Climate-driven trends in contemporary ocean productivity. Nature **444**(7120), 752–755 (2006)

Betts, A.K., Bretherton, C.S., Klinker, E.: Relation between mean boundary-layer structure and cloudiness at the R/V Valdivia during ASTEX. J Atmos Sci **52**(16), 2752–2762 (1995)

Bian, H.S., Zender, C.S.: Mineral dust and global tropospheric chemistry: Relative roles of photolysis and heterogeneous uptake. J. Geophys. Res. **108** D21 (2003).

Blaine, T.W., Keeling, R.F., Paplawsky, W.J.: An improved inlet for precisely measuring the atmospheric Ar/N_2 ratio. Atmos Chem Phys **6**, 1181–1184 (2006)

Bloss, W.J., Evans, M.J., Lee, J.D., Sommariva, R., Heard, D.E., Pilling, M.J.: The oxidative capacity of the troposphere: Coupling of field measurements of OH and a global chemistry transport model. Faraday Discuss. **130**, 425–436 (2005)

Bridgeman, C.H., Pyle, J.A., Shallcross, D.E.: A three-dimensional model calculation of the ozone depletion potential of 1-bromopropane (1-C3H7Br). J. Geophys. Res.-Atmos. **105**(D21), 26493–26502 (2000)

Buck, C.S., Landing, W.M., Resing, J.A., Lebon, G.T.: Aerosol iron and aluminum solubility in the northwest Pacific Ocean: Results from the 2002 IOC cruise. Geochem. Geophy. Geos. **7**, Q04M07 (2006).

Carpenter, L.J., Lewis, A.C., Hopkins, J.R., Read, K.A., Gallagher, M., Longley, I.: Uptake of methanol to the North Atlantic ocean surface. *Global Biogeochem. Cycles*. **18**, (2004).

Chiapello, I., Bergametti, G., Chatenet, B., Bousquet, P., Dulac, F., Santos Soares, E.: Origins of African dust transported over the northeastern tropical Atlantic. J. Geophys. Res. **102**(d12), 13701–13709 (1997)

Chiapello, I., Moulin, C.: TOMS and METEOSAT satellite records of the variability of Saharan dust transport over the Atlantic during the last two decades (1979–1997). Geophys. Res. Lett. **29**(8), 4 (2002)

Commane, R., Floquet, C.F.A., Ingham, T., Stone, D., Evans, M.J., Heard, D.E.: Observations of OH and HO2 radicals over West Africa. Atmos Chem Phys **10**(18), 8783–8801 (2010)

Dall'Osto, M., Harrison, R.M., Highwood, E.J., O'Dowd, C., Ceburnis, D., Querold, X., Achterberge, E.P.: Variation of the mixing state of Saharan dust particles with atmospheric transport. Atmos. Environ. **44** (26), 3135–3146 (2010)

DeCarlo, P., Slowik, J., Worsnop, D.R., Davidovits, P.J.J.: Particle morphology and density characterization by combined mobility and aerodynamic diameter measurements. part 1: Theory. Aerosol Sci. Technol **38**, 1185–1205 (2004)

Dentener, F.J., Carmichael, G.R., Zhang, Y., Lelieveld, J., Crutzen, P.J.: Role of mineral aerosol as a reactive surface in the global atmosphere. J. Geophys. Res. **101**, 22869–22890 (1996)

Deutschmann, T., Beierle, S., Frieß, U., Grzegorski, M., Kern, C., Kritten, L., Pfeilsticker, K., Platt, U., Prados-Roman, C., Pukite, J., Wagner, T., Werner, B.: The Monte Carlo atmospheric radiative tranfer model McArtim: Intruduction and validation of Jacobians and 3D features. J. Quant. Spectrosc. Radiat. Transf. **112**, 1119–1137 (2011)

Duncan, B.N., Martin, R.V., Staudt, A.C., Yevich, R., Logan, J.A.: Interannual and seasonal variability of biomass burning emissions constrained by satellite observations. J. Geophys. Res. **108**(D2) (2003)

Evan, A.T., Vimont, D.J., Heidinger, A.K., Kossin, J.P., Bennartz, R.: The Role of Aerosols in the Evolution of Tropical North Atlantic Ocean Temperature Anomalies. Science **324**(5928), 778–781 (2009)

Facchini, M.C., Rinaldi, M., Decesari, S., Carbone, C., Finessi, E., Mircea, M., Fuzzi, S., Ceburnis, D., Flanagan, R., Nilsson, E.D., de Leeuw, G., Martino, M., Woeltjen, J., O'Dowd, C.D.: Primary submicron marine aerosol dominated by insoluble organic colloids and aggregates. Geophys. Res. Lett. **35**(17), 5 (2008)

Farmer, D.K., Wooldridge, P.J., Cohen, R.C.: Application of thermal-dissociation laser induced fluorescence (TD-LIF) to measurement of HNO3, Σalkyl nitrates, Σperoxy nitrates, and NO2 fluxes using eddy covariance. Atmos Chem Phys **6**(11), 3471–3486 (2006)

Fenter, F.F., Caloz, F., Rossi, M.J.: Experimental-evidence for the efficient dry deposition of nitric-acid on calcite. Atmos. Environ. **29**(22), 3365–3372 (1995)

Fleming, Z.L., Monks, P.S., Rickard, A.R., Heard, D.E., Bloss, W.J., Seakins, P.W., Still, T.J., Sommariva, R., Pilling, M.J., Morgan, R., Green, T.J., Brough, N., Mills, G.P., Penkett, S.A., Lewis, A.C., Lee, J.D., Saiz-Lopez, A., Plane, J.M.C.: Peroxy radical chemistry and the control of ozone photochemistry at Mace Head, Ireland during the summer of 2002. Atmos Chem Phys **6**, 2193–2214 (2006)

Foltz, G.R., McPhaden, M.J.: Impact of Saharan dust on tropical North Atlantic SST. J. Climate **21**(19), 5048–5060 (2008)

Formenti, P., Elbert, W., Maenhaut, W., Haywood, J., Andreae, M.O.: Chemical composition of mineral dust aerosol during the Saharan Dust Experiment (SHADE) airborne campaign in the Cape Verde region, September 2000. J. Geophys. Res. Atmos. **108**, D18 (2003).

Forster, P., Ramaswamy, V., Artaxo, P., Berntsen, T., Betts, R., Fahey, D.W., Haywood, J., Lean, J., Lowe, D. C., Myhre, G., Nganga, J., Prinn, R., Raga, G., Schulz, M., Van Dorland, R.: Changes in atmospheric constituents and in radiative forcing. In: Solomon, S., Qin, D., Manning, M., Chen, Z., Marquis, M., Averyt, K.B., Tignor, M., Miller, H.L. (eds.) Climate change 2007: the physical science basis. Contribution of working group I to the fourth assessment report of the intergovernmental panel on climate change. Cambridge University Press, Cambridge (2007)

Gros, V., Williams, J., Lawrence, M.G., von Kuhlmann, R., van Aardenne, J., Atlas, E., Chuck, A., Edwards, D.P., Stroud, V., Krol, M.: Tracing the origin and ages of interlaced atmospheric pollution events over the tropical Atlantic Ocean with in situ measurements, satellites, trajectories, emission inventories, and global models. J. Geophys. Res. **109**, D22 (2004).

Guenther, A., Hewitt, C.N., Erickson, D., Fall, R., Geron, C., Gradel, T., Harley, P., Klenger, L., Lerdau, M., Mckay, W.A., Pierce, T., Scholes, B., Steinbrecher, R., Tallamraju, R., Taylor, R.J., Zimmerman, P.: A global model of natural volatile organic compound emissions. J. Geophys. Res. **100**(d5), 8873–8892 (1995)

Guieu, C., Loÿe-Pilot, M.D., Ridame, C., Thomas, C.: Chemical characterization of the Saharan dust end-member: Some biogeochemical implications for the western Mediterranean Sea. J. Geophys. Res. **107**, (2002).

Hagen, E.: Northwest African upwelling scenario. Oceanol. Acta **24**, S113–S128 (2001)

Hanisch, F., Crowley, J.N.: Heterogeneous reactivity of gaseous nitric acid on Al2O3, CaCO3, and atmospheric dust samples: A Knudsen cell study. J. Phys. Chem. A **105**(13), 3096–3106 (2001)

Hanisch, F., Crowley, J.N.: Heterogeneous reactivity of NO and HNO3 on mineral dust in the presence of ozone. Phys. Chem. Chem. Phys. **5**(5), 883–887 (2003)

Hanson, H.P.: Marine stratocumulus climatologies. Int. J. Climatol. **11**(2), 147–164 (1991)

Hao, W.M., Ward, D.E., Olbu, G., Baker, S.P.: Emissions of CO2, CO, and hydrocarbons from fires in diverse African savanna ecosystems. J. Geophys. Res. **101**(D19), 23577–23584 (1996)

Heard, D.E., Pilling, M.J.: Measurement of OH and HO_2 in the Troposphere. Chem. Rev. **103**, 5163–5198 (2003)

Heinold, B., Helmert, J., Hellmuth, O., Wolke, R., Ansmann, A., Marticorena, B., Laurent, B., Tegen, I.: Regional modeling of Saharan dust events using LM-MUSCAT: Model description and case studies. J Geophys Res. **112**, D11 (2007).

Heinold, B., Tegen, I., Bauer, S., Wendisch, M.: Regional modelling of radiative effects and feedbacks of Saharan dust and biomass burning aerosol. Tellus B. **63**, 800–813 (2011)

Helmig, D., Bottenheim, J., Galbally, I.E., Lewis, A., Milton, M.J.T., Penkett, S., Plass-Duelmer, C., Reimann, S., Tans, P. and Theil, S., 2009: Volatile Organic Compounds in the Global Atmosphere. Eos Trans. AGU. **90**, 52 (2009).

Herut, B., Collier, R., Krom, M.D.: The role of dust in supplying nitrogen and phosphorus to the Southeast Mediterranean. Limnol. Oceanogr. **47**(3), 870–878 (2002)

Hewitt, C.N., Lee, J.D., MacKenzie, A.R., Barkley, M.P., Carslaw, N., Carver, G.D., Chappell, N.A., Coe, H., Collier, C., Commane, R., Davies, F., Davison, B., Di Carlo, P., Di Marco, C.F., Dorsey, J.R., Edwards, P.M., Evans, M.J., Fowler, D., Furneaux, K.L., Gallagher, M., Guenther, A., Heard, D.E., Helfter, C., Hopkins, J., Ingham, T., Irwin, M., Jones, C., Karunaharan, A., Langford, B., Lewis, A.C., Lim, S.F., MacDonald, S.M., Mahajan, A.S., Malpass, S., McFiggans, G., Mills, G., Misztal, P., Moller, S., Monks, P.S., Nemitz, E., Nicolas-Perea, V., Oetjen, H., Oram, D.E., Palmer, P.I., Phillips, G.J., Pike, R., Plane, J.M.C., Pugh, T., Pyle, J.A., Reeves, C.E., Robinson, N.H., Stewart, D., Stone, D., Whalley, L.K., Yin, X.: Overview: oxidant and particle photochemical processes above a south-east Asian tropical rainforest (the OP3 project): introduction, rationale, location characteristics and tools. Atmos Chem Phys **10**(1), 169–199 (2010)

Holloway, J.S., Jakoubek, R.O., Parrish, D.D., Gerbig, C., Volz-Thomas, A., Schmitgen, S., Fried, A., Wert, B., Henry, B., Drummond, J.R.: Airborne intercomparison of vacuum ultraviolet fluorescence and tunable diode laser absorption measurements of tropospheric carbon monoxide. J. Geophys. Res.-Atmos. **105**(D19), 24251–24261 (2000)

Hopkins, J.R., Lewis, A.C., Read, K.A.: A two-column method for long-term monitoring of non-methane hydrocarbons (NMHCs) and oxygenated volatile organic compounds (o-VOCs). J. Environ. Monit. **5**(1), 8–13 (2003)

Horowitz, L.W., Walters, S., Mauzerall, D.L., Emmons, L.K., Rasch, P.J., Granier, C., Tie, X.X., Lamarque, J.F., Schultz, M.G., Tyndall, G.S., Orlando, J.J. and Brasseur, G.P., 2003: A global simulation of tropospheric ozone and related tracers: Description and evaluation of MOZART, version 2. J. Geophys. Res. **108**, D24 (2003).

Hosaynali Beygi, Z., Fischer, H., Harder, H.D., Martinez, M., Sander, R., Williams, J., Brookes, D.M., Monks, P.S., Lelieveld, J.: Oxidation photochemistry in the Southern Atlantic boundary layer: unexpected deviations of photochemical steady state. Atmos. Chem. Phys. Discuss. **11**(3), 7045–7093 (2011)

Huneeus, N., Schulz, M., Balkanski, Y., Griesfeller, J., Kinne, S., Prospero, J., Bauer, S., Boucher, O., Chin, M., Dentener, F., Diehl, T., Easter, R., Fillmore, D., Ghan, S., Ginoux, P., Grini, A., Horowitz, L., Koch, D., Krol, M.C., Landing, W., Liu, X., Mahowald, N., Miller, R.L., Morcrette, J.-J., Myhre, G., Penner, J. E., Perlwitz, J.P., Stier, P., Takemura, T., Zender, C.: Global dust model intercomparison in AeroCom phase I. Atmos Chem Phys **11**(15), 7781–7816 (2011)

Jacob, D.J., Field, B.D., Jin, E.M., Bey, I., Li, Q.B., Logan, J.A., Yantosca, R.M., Singh, H.B.: Atmospheric budget of acetone. J. Geophys. Res. **107**(D10), 4100 (2002)

Jacobi, H.W., Weller, R., Bluszcz, T., Schrems, O.: Latitudinal distribution of peroxyacetyl nitrate (PAN) over the Atlantic Ocean. J. Geophys. Res.-Atmos. **104**(D21), 26901–26912 (1999)

Jiménez-Vélez, B., Detres, Y., Armstrong, R.A., Gioda, A.: Characterization of African Dust (PM2.5) across the Atlantic Ocean during AEROSE 2004. Atmos. Environ. **43**(16), 2659–2664 (2009)

Jones, C.E., Hornsby, K.E., Sommariva, R., Dunk, R.M., Von Glasow, R., McFiggans, G., Carpenter, L.J.: Quantifying the contribution of marine organic gases to atmospheric iodine. Geophys. Res. Lett. **37** (2010). doi:10.1029/2010gl043990

Journet, E., Desboeufs, K.V., Caquineau, S., Colin, J.L.: Mineralogy as a critical factor of dust iron solubility. Geophys. Res. Lett. **35**(7), 5 (2008)

Kalnay, E., Kanamitsu, M., Kistler, R., Collins, W., Deaven, D., Gandin, L., Iredell, M., Saha, S., White, G., Woollen, J., Zhu, Y., Leetmaa, A., Reynolds, R., Chelliah, M., Ebisuzaki, W., Higgins, W., Janowiak, J., Mo, K.C., Ropelewski, C., Wang, J., Jenne, R., Joseph, D.: The NCEP/NCAR 40-Year Reanalysis Project. Bull. Am. Meteorol. Soc. **77**(3), 437–471 (1996)

Kandler, K., Benker, N., Bundke, U., Cuevas, E., Ebert, M., Knippertz, P., Rodríguez, S., Schütz, L., Weinbruch, S.: Chemical composition and complex refractive index of Saharan Mineral Dust at Izaña, Tenerife (Spain) derived by electron microscopy. Atmos. Environ. **41**(37), 8058–8074 (2007)

Kaufman, Y.J., Koren, I., Remer, L.A., Tanre, D., Ginoux, P., Fan, S.: Dust transport and deposition observed from the Terra-Moderate Resolution Imaging Spectroradiometer (MODIS) spacecraft over the Atlantic ocean. J. Geophys. Res. **110**, D10 (2005).

Kock, A., Gebhardt, S., Bange, H.W.: Methane emissions from the upwelling area off Mauritania (NW Africa). Biogeosciences **5**(4), 1119–1125 (2008)

Kozlova, E.A., Manning, A.C.: Methodology and calibration for continuous measurements of biogeochemical trace gas and O_2 concentrations from a 300-m tall tower in central Siberia. Atmos Meas Tech **2**(1), 205–220 (2009)

Kurten, T., Loukonen, V., Vehkamaki, H., Kulmala, M.: Amines are likely to enhance neutral and ion-induced sulfuric acid-water nucleation in the atmosphere more effectively than ammonia. Atmos Chem Phys **8**(14), 4095–4103 (2008)

Lawler, M.J., Finley, B.D., Keene, W.C., Pszenny, A.A.P., Read, K.A., von Glasow, R., Saltzman, E.S.: Pollution-enhanced reactive chlorine chemistry in the eastern tropical Atlantic boundary layer. Geophys. Res. Lett. **36** (2009). doi:10.1029/2008GL036666

Lawrence, M.G., Jöckel, P., von Kuhlmann, R.: What does the global mean OH concentration tell us? Atmos Chem Phys **1**(1), 37–49 (2001)

Lee, J.D., McFiggans, G., Allan, J.D., Baker, A.R., Ball, S.M., Benton, A.K., Carpenter, L.J., Commane, R., Finley, B.D., Evans, M., Fuentes, E., Furneaux, K., Goddard, A., Good, N., Hamilton, J.F., Heard, D.E., Herrmann, H., Hollingsworth, A., Hopkins, J.R., Ingham, T., Irwin, M., Jones, C.E., Jones, R.L., Keene, W.C., Lawler, M.J., Lehmann, S., Lewis, A.C., Long, M.S., Mahajan, A., Methven, J., Moller, S.J., Muller, K., Muller, T., Niedermeier, N., O'Doherty, S., Oetjen, H., Plane, J.M.C., Pszenny, A.A.P., Read, K.A., Saiz-Lopez, A., Saltzman, E.S., Sander, R., von Glasow, R., Whalley, L., Wiedensohler, A., Young, D.: Reactive Halogens in the Marine Boundary Layer (RHaMBLe): the tropical North Atlantic experiments. Atmos Chem Phys **10**(3), 1031–1055 (2010)

Lee, J.D., Moller, S.J., Read, K.A., Lewis, A.C., Mendes, L., Carpenter, L.J.: Year-round measurements of nitrogen oxides and ozone in the tropical North Atlantic marine boundary layer. J. Geophys. Res. **114** (2009). doi:10.1029/2009jd011878

Lewis, A.C., Evans, M.J., Methven, J., Watson, N., Lee, J.D., Hopkins, J.R., Purvis, R.M., Arnold, S.R., McQuaid, J.B., Whalley, L.K., Pilling, M.J., Heard, D.E., Monks, P.S., Parker, A.E., Reeves, C.E., Oram, D.E., Mills, G., Bandy, B.J., Stewart, D., Coe, H., Williams, P., Crosier, J.: Chemical composition observed over the mid-Atlantic and the detection of pollution signatures far from source regions. J. Geophys. Res. **112**, D10 (2007).

Lewis, A.C., Hopkins, J.R., Carpenter, L.J., Stanton, J., Read, K.A., Pilling, M.J.: Sources and sinks of acetone, methanol, and acetaldehyde in North Atlantic marine air. Atmos Chem Phys **5**, 1963–1974 (2005)

Liao, H., Seinfeld, J.H.: Global impacts of gas-phase chemistry-aerosol interactions on direct radiative forcing by anthropogenic aerosols and ozone. J. Geophys. Res. **110**, 18208 (2005)

Lilly, D.K.: Models of cloud-topped mixed layers under a strong inversion. Q. J. Roy. Meteor. Soc. **94**, 292–309 (1968)

Loukonen, V., Kurten, T., Ortega, I.K., Vehkamaki, H., Padua, A.A.H., Sellegri, K., Kulmala, M.: Enhancing effect of dimethylamine in sulfuric acid nucleation in the presence of water - a computational study. Atmos Chem Phys **10**(10), 4961–4974 (2010)

Mahajan, A.S., Plane, J.M.C., Oetjen, H., Mendes, L., Saunders, R.W., Saiz-Lopez, A., Jones, C.E., Carpenter, L.J., McFiggans, G.B.: Measurement and modelling of tropospheric reactive halogen species over the tropical Atlantic Ocean. Atmos Chem Phys **10**(10), 4611–4624 (2010a)

Mahajan, A.S., Whalley, L.K., Kozlova, E.A., Oetjen, H., Mendez, L., Furneaux, K.L., Goddard, A., Heard, D.E., Plane, J.M.C., Saiz-Lopez, A.: DOAS observations of formaldehyde and its impact on the HOx balance in the tropical Atlantic marine boundary layer. J Atmos Chem **66**(3), 167–178 (2010b)

Mahowald, N.M., Baker, A.R., Bergametti, G., Brooks, N., Duce, R.A., Jickells, T.D., Kubilay, N., Prospero, J.M., Tegen, I.: Atmospheric global dust cycle and iron inputs to the ocean. Global Biogeochem. Cycles **19**(4) (2005)

Makela, J.M., Yli-Koivisto, S., Hiltunen, V., Seidl, W., Swietlicki, E., Teinila, K., Sillanpaa, M., Koponen, I. K., Paatero, J., Rosman, K., Hameri, K.: Chemical composition of aerosol during particle formation events in boreal forest. Tellus B Chem. Phys. Meteorol. **53**(4), 380–393 (2001)

Manning, A.C., Keeling, R.F.: Global oceanic and land biotic carbon sinks from the Scripps atmospheric oxygen flask sampling network. Tellus B Chem. Phys. Meteorol. **58**(2), 95–116 (2006)

Martínez Avellaneda, N., Serra, N., Minnett, P.J., Stammer, D.: Response of the eastern subtropical Atlantic SST to Saharan dust: A modeling and observational study. J. Geophys. Res. **115**(C8), C08015 (2010)

Measures, C.I., Vink, S.: On the use of dissolved aluminum in surface waters to estimate dust deposition to the ocean. Global Biogeochem. Cycles **14**(1), 317–327 (2000)

Merten, A., Tschritter, J., Platt, U.: Design of differential optical absorption spectroscopy long-path telescopes based on fiber optics. Appl. Opt. **50**(5), 738–754 (2011)

Millet, D.B., Jacob, D.J., Custer, T.G., de Gouw, J.A., Goldstein, A.H., Karl, T., Singh, H.B., Sive, B.C., Talbot, R.W., Warneke, C., Williams, J.: New constraints on terrestrial and oceanic sources of atmospheric methanol. Atmospheric Chemistry & Physics **8**(23), 6887–6905 (2008)

Millet, D.B., Guenther, A., Siegel, D.A., Nelson, N.B., Singh, H.B., de Gouw, J.A., Warneke, C., Williams, J., Eerdekens, G., Sinha, V., Karl, T., Flocke, F., Apel, E., Riemer, D.D., Palmer, P.I., Barkley, M.: Global atmospheric budget of acetaldehyde: 3-D model analysis and constraints from in-situ and satellite observations. Atmos Chem Phys **10**(7), 3405–3425 (2010)

Mills, M.M., Ridame, C., Davey, M., La Roche, J., Geider, R.J.: Iron and phosphorus co-limit nitrogen fixation in the eastern tropical North Atlantic. Nature **429**(6989), 292–294 (2004)

Monks, P.S.: Gas-phase radical chemistry in the troposphere. Chem. Soc. Rev. **34**(5), 376–395 (2005)

Monks, P.S., Carpenter, L.J., Penkett, S.A., Ayers, G.P.: Night-time peroxy radical chemistry in the remote marine boundary layer over the Southern ocean. Geophys. Res. Lett. **23**(5), 535–538 (1996)

Monks, P.S., Salisbury, G., Holland, G., Penkett, S.A., Ayers, G.P.: A seasonal comparison of ozone photochemistry in the remote marine boundary layer. Atmos. Environ. **34**(16), 2547–2561 (2000)

Moore, C.M., Mills, M.M., Achterberg, E.P., Geider, R.J., LaRoche, J., Lucas, M.I., McDonagh, E.L., Pan, X., Poulton, A.J., Rijkenberg, M.J.A., Suggett, D.J., Ussher, S.J., Woodward, E.M.S.: Large-scale distribution of Atlantic nitrogen fixation controlled by iron availability. Nat. Geosci. **2**(12), 867–871 (2009)

Morel, F.M.M., Hering, J.G.: Principles and applications of aquatic chemistry, vol 2. Wiley, New York (1993)

Moulin, C., Lambert, C.E., Dulac, F., Dayan, U.: Control of atmospheric export of dust from North Africa by the North Atlantic oscillation. Nature **387**(6634), 691–694 (1997)

Müller, C., Iinuma, Y., Karstensen, J., van Pinxteren, D., Lehmann, S., Gnauk, T., Herrmann, H.: Seasonal variation of aliphatic amines in marine sub-micrometer particles at the Cape Verde islands. Atmos Chem Phys **9**(24), 9587–9597 (2009)

Müller, K., Lehmann, S., van Pinxteren, D., Gnauk, T., Niedermeier, N., Wiedensohler, A., Herrmann, H.: Particle characterization at the Cape Verde atmospheric observatory during the 2007 RHaMBLe intensive. Atmos Chem Phys **10**(6), 2709–2721 (2010)

Olivier, J., Bouwman, A., Maas, C. v. d., Berdowski, J., Veldt, C., Bloos, J., Visschedijk, A., Zandveld, P., Haverlag, J.: Description of EDGAR Version 2.0: A set of global emission inventories of greenhouse gases and ozone-depleting substances for all anthropogenic and most natural sources on a per country basis and on 1 degree x 1 degree grid. Natl. Inst. of Public Health and the Environ., Bilthoven, Netherlands. (1996).

Parrish, D.D., Buhr, M.P., Trainer, M., Norton, R.B., Shimshock, J.P., Fehsenfeld, F.C., Anlauf, K.G., Bottenheim, J.W., Tang, Y.Z., Wiebe, H.A., Roberts, J.M., Tanner, R.L., Newman, L., Bowersox, V.C., Olszyna, K.J., Bailey, E.M., Rodgers, M.O., Wang, T., Berresheim, H., Roychowdhury, U.K., Demerjian, K.L.: The total recative nitrogen levels and the partititioning between the individual-species at 6 rural sites in eastern North America. J. Geophys. Res. **98**(D2), 2927–2939 (1993)

Parrish, D.D., Trainer, M., Holloway, J.S., Yee, J.E., Warshawsky, M.S., Fehsenfeld, F.C., Forbes, G.L., Moody, J.L.: Relationships between ozone and carbon monoxide at surface sites in the North Atlantic region. J. Geophys. Res. **103**(D11), 13357–13376 (1998)

Plane, J.M., Saiz-Lopez, A.: Differential optical absorption spectroscopy, in analytical techniques for atmospheric measurement. Blackwell, Oxford (2006)

Prospero, J.M., Lamb, P.J.: African droughts and dust transport to the Caribbean: Climate change implications. Science **302**, 1,024–021,027 (2003)

Prospero, J.M., Ginoux, P., Torres, O., Nicholson, S.E., Gill, T.E.: Environmental characterization of global sources of atmospheric soil dust identified with the NIMBUS 7 total ozone mapping spectrometer (TOMS) absorbing aerosol product. Rev. Geophys. **40**, 1002 (2002)

Read, K.A., Mahajan, A.S., Carpenter, L.J., Evans, M.J., Faria, B.V.E., Heard, D.E., Hopkins, J.R., Lee, J.D., Moller, S.J., Lewis, A.C., Mendes, L., McQuaid, J.B., Oetjen, H., Saiz-Lopez, A., Pilling, M.J., Plane, J. M.C.: Extensive halogen-mediated ozone destruction over the tropical Atlantic Ocean. Nature **453** (7199), 1232–1235 (2008)

Read, K.A., Lee, J.D., Lewis, A.C., Moller, S.J., Mendes, L., Carpenter, L.J.: Intra-annual cycles of NMVOC in the tropical marine boundary layer and their use for interpreting seasonal variability in CO. J. Geophys. Res. **114** (2009). doi:10.1029/2009jd011879

Real, E., Law, K.S., Schlager, H., Roiger, A., Huntrieser, H., Methven, J., Cain, M., Holloway, J., Neuman, J. A., Ryerson, T., Flocke, F., de Gouw, J., Atlas, E., Donnelly, S., Parrish, D.: Lagrangian analysis of low altitude anthropogenic plume processing across the North Atlantic. Atmos Chem Phys **8**(24), 7737–7754 (2008)

Reeves, C.E., Penkett, S.A.: Measurements of peroxides and what they tell us. Chem. Rev. **103**(12), 5199–5218 (2003)

Richardson, A.J., Schoeman, D.S.: Climate impact on plankton ecosystems in the Northeast Atlantic. Science **305**(5690), 1609–1612 (2004)

Richter, A., Burrows, J.P.: Tropospheric NO2 from GOME measurements. Adv. Space Res. **29**(11), 1673–1683 (2002)

Ryall, D.B., Derwent, R.G., Manning, A.J., Simmonds, P.G., O'Doherty, S.: Estimating source regions of European emissions of trace gases from observations at Mace Head. Atmos. Environ. **35**(14), 2507–2523 (2001)

Savoie, D.L., Prospero, J.M., Oltmans, S.J., Graustein, W.C., Turekian, K.K., Merrill, J.T., Levy, H.: Sources of nitrate and ozone in the marine boundary-layer of the tropical North-Atlantic. J. Geophys. Res. **97** (D11), 11575–11589 (1992)

Schepanski, K., Tegen, I., Macke, A.: Saharan dust transport and deposition towards the tropical northern Atlantic. Atmos Chem Phys **9**(4), 1173–1189 (2009)

Severinghaus, J.P.: Studies of the terrestrial O_2 and carbon cycles in sand dune gases and in Biosphere 2. Ph. D., Columbia University (1995)

Sholkovitz, E.R., Sedwick, P.N., Church, T.M.: Influence of anthropogenic combustion emissions on the deposition of soluble aerosol iron to the ocean: Empirical estimates for island sites in the North Atlantic. Geochimica Et Cosmochimica Acta **73**(14), 3981–4003 (2009)

Simmonds, P.G., Derwent, R.G.: Measurements of ozone and other radiatively active gases at Mace Head in the Republic of Ireland. Atmos. Environ. **25**(9), 1795–1808 (1991)

Singh, H.B., Kanakidou, M., Crutzen, P., Jacob, D.: High concentrations and photochemistry of carbonyls and alcohols in the global troposphere. Nature **378**, 50–54 (1995)

Sinha, V., Williams, J., Meyerhöfer, M., Riebesell, U., Paulino, A.I., Larsen, A.: Air-sea fluxes of methanol, acetone, acetaldehyde, isoprene and DMS from a Norwegian fjord following a phytoplankton bloom in a mesocosm experiment. Atmos Chem Phys **7**(3), 739–755 (2007)

Smith, J.N., Barsanti, K.C., Friedli, H.R., Ehn, M., Kulmala, M., Collins, D.R., Scheckman, J.H., Williams, B.J., McMurry, P.H.: Observations of aminium salts in atmospheric nanoparticles and possible climatic implications. Proc. Natl. Acad. Sci. U. S. A. **107**(15), 6634–6639 (2010)

Sokolik, I.N., Toon, O.B.: Direct radiative forcing by anthropogenic airborne mineral aerosols. Nature **381** (6584), 681–683 (1996)

Stephens, B.B., Keeling, R.F., Heimann, M., Six, K.D., Murnane, R., Caldeira, K.: Testing global ocean carbon cycle models using measurements of atmospheric O_2 and CO_2 concentration. Global Biogeochem. Cycles **12**(2), 213–230 (1998)

Stewart, D.J., Taylor, C.M., Reeves, C.E., McQuaid, J.B.: Biogenic nitrogen oxide emissions from soils: impact on NOx and ozone over west Africa during AMMA (African Monsoon Multidisciplinary Analysis): observational study. Atmos Chem Phys **8**(8), 2285–2297 (2008)

Stramma, L., Brandt, P., Schafstall, J., Schott, F., Fischer, J., Kortzinger, A.: Oxygen minimum zone in the North Atlantic south and east of the Cape Verde Islands. J. Geophys. Res. **113**(C4), C04014 (2008)

Stull, R.B.: An introduction to boundary layer meteorology. Kluwer Academic Publishers, Dordrecht (1988)

Taddei, S., Toscano, P., Gioli, B., Matese, A., Miglietta, F., Vaccari, F.P., Zaldei, A., Custer, T., Williams, J.: Carbon Dioxide and Acetone Air-Sea Fluxes over the Southern Atlantic. Environ. Sci. Technol. **43**, 5 (2009)

Tie, X.X., Madronich, S., Walters, S., Edwards, D.P., Ginoux, P., Mahowald, N., Zhang, R.Y., Lou, C., Brasseur, G.: Assessment of the global impact of aerosols on tropospheric oxidants. J. Geophys. Res. **110**, D3 (2005).

Tuch, T.M., Haudek, A., Mueller, T., Nowak, A., Wex, H., Wiedensohler, A.: Design and performance of an automatic regenerating adsorption aerosol dryer for continuous operation at monitoring sites. Atmos Meas Tech **2**(2), 417–422 (2009)

Vaughan, S., Ingham, T., Whalley, L.K., Stone, D., Evans, M.J., Read, K.A., Lee, J.D., Moller, S.J., Carpenter, L.J., Lewis, A.C., Fleming, Z.L., Heard, D.E.: Seasonal observations of OH and HO2 in the remote tropical marine boundary layer *Atmos*. Chem. Phys. Discuss. **11**(7), 21429–21487 (2011)

Wang, S.C., Flagan, R.C.: Scanning Electrical Mobility Spectrometer. J. Aerosol Sci. **20**, 1485–1488 (1989)

Whalley, L.K., Furneaux, K.L., Goddard, A., Lee, J.D., Mahajan, A., Oetjen, H., Read, K.A., Kaaden, N., Carpenter, L.J., Lewis, A.C., Plane, J.M.C., Saltzman, E.S., Wiedensohler, A., Heard, D.E.: The chemistry of OH and HO2 radicals in the boundary layer over the tropical Atlantic Ocean. Atmos Chem Phys **10**(4), 1555–1576 (2010)

Yienger, J.J., Levy, H.: Empirical-model of global soil-biogenic NOx emissions. J. Geophys. Res.-Atmos. **100**(D6), 11447–11464 (1995)

Zeng, X.B., Brunke, M.A., Zhou, M.Y., Fairall, C., Bond, N.A., Lenschow, D.H.: Marine atmospheric boundary layer height over the eastern Pacific: Data analysis and model evaluation. J. Climate **17**(21), 4159–4170 (2004)